POLITECNICO DI MILANO

Scuola di Ingegneria Industriale e dell'Informazione

Corso di Laurea Magistrale in Ingegneria Fisica

APPROACHING GREEN MATERIALS FOR PHOTOVOLTAICS: BISMUTH(III) SULFIDE AND COPPER(I) SULFIDE IN HYBRID SOLAR CELLS

Relatore:

Prof. Guglielmo Lanzani

Correlatrice:

Dott.ssa Annamaria Petrozza

Tesi di laurea di:

Giulio Mazzotta

matr. 780794

Anno Accademico 2013/2014

Ringraziamenti
Acknowledgments

Arrivati alla fine di questo lungo e faticoso percorso, credo sia doveroso esprimere un pensiero di ringraziamento a coloro che mi hanno permesso di tagliare questo traguardo.

Inzio ringraziando il Prof. Guglielmo Lanzani che mi ha permesso di svolgere la tesi presso il CNST IIT, un meraviglioso posto dove è riuscito a creare il giusto connubio di professionalità e informalità, rendendolo un luogo dove si lavora ad alto livello seppur in un clima straordinariamente rilassante, amichevole e divertente.

Un grazie speciale ad Anna che mi ha accolto nel fantastico gruppo che dirige, per avermi permesso di imparare tanto, per gli innumerevoli consigli e aiuti per il presente e per il futuro, e per avermi sempre fatto sentire apprezzato; per tutta la durata di questo lavoro mi ha fatto uscire di casa ogni mattina entusiasta di ciò che andavo a fare. Un grazie quindi ai membri di questo gruppo, a cominciare da quelli con cui ho lavorato più a stretto contatto: Maddy, che mi ha insegnato l'abc della vita in laboratorio; Simo, sempre iperdisponibile e pronto a risolvere ogni mio dubbio anche a 2000 km di distanza; Michele, con cui ho passato i momenti più divertenti in laboratorio; Marina, che entrata da poco ha portato un'ulteriore ventata di allegria al gruppo e gli ultimi arrivati Chen e James, che nonostante non siano qui da molto, il tempo è comunque bastato per ricevere qualche prezioso consiglio anche da loro; e poi ci sono i "Petrozzcopists", Ajay, Giulia, Marcelo, Ilaria, Tomas, Stefanie, con cui ho lavorato meno ma che fra pranzi, caffè e group meeting hanno reso estremamente piacevoli questi mesi, e soprattutto Valerio, che prima che dottorando di questo gruppo è stato compagno di studi, e alla cui disponibilità e incredibili capacità calligrafiche devo buona parte della riuscita dei miei esami (chissà se sarei qua senza i suoi appunti!).

Un ringraziamento poi a tutti i membri del CNST, amici sempre disponibili a dare consigli e suggerimenti sul piano lavorativo, e divertenti compagni di pranzi,

caffè, gite e grigliate. I mesi passati in questo posto resteranno fra i più piacevoli che potrò mai ricordare.

Un grazie particolare va dunque ad Andrei, amico di una vita, che anche in questo lavoro mi ha aiutato con innumerevoli consigli di scrittura e correzioni.

E infine un ringraziamento va alla famiglia e agli amici, persone non strettamente legate a questo lavoro ma fondamentali nella mia vita e quindi anche in questo traguardo, a cui non voglio dedicare qualche banale frase di circostanza ma a cui inevitabilmente va il mio pensiero mentre scrivo questa pagina.

Contents

Contents **v**

List of Figures **vii**

List of Tables **ix**

Abstract **xi**

Sommario – *Italian abstract* **xiii**

Estratto – *Italian extract* **xv**

List of Abbreviations **xxiv**

Introduction **1**

1 New generation green photovoltaic **3**
- 1.1 Introduction . . . 3
- 1.2 "Conventional" solar cells . . . 3
  - 1.2.1 Thin Films: Copper Indium Gallium (di)selenide (CIGS) . . . 7
- 1.3 Excitonic Solar Cells . . . 10
  - 1.3.1 Organic Photovoltaic . . . 13
  - 1.3.2 Dye Sensitized Solar Cells (DSCs) . . . 18
  - 1.3.3 Quantum Dots Solar Cells . . . 23
- 1.4 Benchmark parameters . . . 26
  - 1.4.1 Short Circuit current density (J_{SC}) . . . 27
  - 1.4.2 Open Circuit Voltage (V_{OC}) . . . 27
  - 1.4.3 Fill Factor (FF) . . . 28
  - 1.4.4 Power Conversion Efficiency (PCE) . . . 29

2 Materials and methods **31**
2.1 Introduction . . . 31
2.2 Solar cells based on bismuth(III) sulfide . . . 31
2.2.1 Device structure . . . 32
2.2.2 Experimental . . . 35
2.3 Copper(I) sulfide . . . 42
2.3.1 Material properties . . . 42
2.3.2 Experimental . . . 43

3 Results **47**
3.1 Solar cells with bismuth(III) sulfide . . . 47
3.1.1 Run 1: Test of architectures . . . 47
3.1.2 Experiment 2: Optimized solution . . . 52
3.1.3 Run 3: Bulk etherojunction . . . 55
3.2 Copper sulfide deposition . . . 57

4 Conclusions and outlooks **61**

Bibliography **63**

List of Figures

1 Immagine delle strutture testate con il Bi_2S_3. xvi
2 V_{oc}, J_{ss}, FF e PCE ottenuti nel primo esperimento con il solfuro di bismuto. xviii
3 V_{oc}, J_{ss}, FF e PCE ottenuti nel secondo esperimento con il solfuro di bismuto. xix
4 V_{oc}, J_{ss}, FF e PCE ottenuti nel terzo esperimento con il solfuro di bismuto. xx
5 Confronto degli spettri di assorbimento di Cu_XS deposti su diversi substrati. xxi

1.1 Schematic band diagram of a conventional solar cell. 5
1.2 Schematic cross section of a typical Cu(InGa)Se_2 solar cell. 9
1.3 Band diagram of a ZnO/CdS/Cu(InGa)Se_2 device at 0 V in the dark. 9
1.4 Jablosnki diagram in the optically excited molecule 10
1.5 Multistep charge photogeneration process. 11
1.6 Schematic picture of the donor acceptor interface 12
1.7 Picture of hybrid orbitals 13
1.8 Dispersion diagram of a chain of equal spaced carbon atoms and of a chain of atoms close in couples. 15
1.9 Schematic cross-section of nanomorphologies of bulk heterojunction solar cells. 16
1.10 Different device architectures of bulk heterojunction solar cells. . . 17
1.11 Schematic representation of a liquid Dye Sensitized Solar Cell . . 19
1.12 Schematic energy diagram for the electronic processes and main loss mechanisms in the solid-state dye-sensitized solar cell. 20

1.13 Three-dimensional schematic representation of perovskite structure, Cartoon illustrating the charge transfer and transport in a perovskite sensitized TiO2 solar cell and schematic representation of full device structure, where the mesoporous oxide is either Al2O3 or anatase TiO2 22
1.14 Multi Exciton Generation (MEG) via impact ionization process . 24
1.15 Energy levels vs vacuum of various metal-chalcogenide quantum dots (QDs) 25

2.1 Single crystal structure of Bi_2S_3 32
2.2 Picture of structures tested with Bi_2S_3. 33
2.3 Band diagram of the planar heterojunction structure. 34
2.4 Band diagram of the structure with the TiO_2 layer 35
2.5 Schematic picture of patterned glass slides 37
2.6 Typical set-up for the electrical characterization of a solar cell . . 41
2.7 Structural formulas of precursors used in copper sulfide deposition 43
2.8 Schematic picture of the integrating sphere used in the spectrophotometer 45

3.1 V_{oc}, J_{ss}, FF and PCE values obtained in first experiment with solar cells with bismuth sulfide. 50
3.2 JV curves of devices realized with bismuth sulfide. 51
3.3 V_{oc}, J_{ss}, FF and PCE values obtained in second experiment with solar cells with bismuth sulfide. 52
3.4 SEM image of the solar cell. 53
3.5 SEM image, detail of the Bi_2S_3/mp-TiO_2 interface 54
3.6 V_{oc}, J_{ss}, FF and PCE values obtained in third experiment with solar cells with bismuth sulfide. 55
3.7 Absorbance spectra of deposed Cu_xS 57
3.8 Comparison of Cu_2S spectra deposed on different substrates with same annealing treatment. 59

List of Tables

1.1 Most important intrinsic defects for device-quality $CuInSe_2$ 8

2.1 Screen printer parameters for mesoporous TiO_2 layer deposition . 38

3.1 Summary of cell performace 48

Abstract

The increasing role of photovoltaics as a possible answer to the need of a sustainable source of energy has brought research to face several challenges in order to overtake conventional silicon based solar cells and move towards a cheap, performing and eco-friendly photovoltaics. In this work two promising toxic-free and earth-abundant materials, bismuth(III) sulfide and copper(I) sulfide, have been tested as potentially light absorber in solar cells.

Bismuth sulfide (Bi_2S_3) has been tested in several devices structures, and the fabricated cells have been characterized with JV measurements under simulated solar light. The first architecture is a planar structure composed by Bi_2S_3 deposed on a transparent conductive oxide (TCO) and covered by a hole tranporting material (P3HT or spiro-OMeTAD). In the second architecture a hole blocking layer of compact TiO_2 was added between Bi_2S_3 and TCO. In the third structure, a mesoporous layer of TiO_2 was added on the compact TiO_2 layer to provide a scaffold for nanocrystals of Bi_2S_3. Finally, a structure with a mesoporous layer of TiO_2 coated with a blend of nanocrystals dispersed in P3HT has been tried. The last structure resulted in the best performances, showing an open circuit voltage of 0.61 V, a short circuit current density of 1,05 mA/cm^2, a fill factor of 42,7% and a power conversion efficiency of 0.28%.

Experiments with Copper(I) Sulphide regarded the synthesis procedures. A new technique for a solution process deposition has been tried using a metal salt, copper(I) acetate as copper source, thiourea as sulfur source and pyridine as solvent. Precursors have been deposed via spin coating on different substrates,

FTO coated glass, compact TiO_2 and mesoporous TiO_2, and samples have been optically characterized with a spectrophotometer.

Absorption spectra demonstrate that this actual technique lead to a mixed phase and needs to be optimized to obtain a pure copper(I) sulphide.

Sommario
Italian abstract

Il ruolo crescente del fotovoltaico come possibile risposta al bisogno di una risorsa sostenibile di energia ha portato la ricerca ad affrontare diverse sfide per superare la tecnologia tradizionale basata sul silicio e puntare ad un nuovo fotovoltaico ecologico, economico e performante. In questo lavoro sono stati testati due promettenti materiali atossici e abbondanti in nautra, solfuro di bismuto(III) e solfuro di rame(I), per il loro possibile uso come assorbitori di luce in celle solari.

Il solfuro di bismuto (Bi_2S_3) è stato testato in dispositivi con varie architetture, e le celle fabbricate sono state caratterizzate con misure JV sotto luce solare simulata. La prima architettura è composta da Bi_2S_3 deposto su un ossido conduttivo trasparente (TCO) e coperta da un materiale trasportatore di lacune (P3HT o spiro-OMeTAD). Nella seconda architettura uno strato blocca lacune composto da TiO_2 compatto è stato aggiunto fra il Bi_2S_3 e il TCO. Nella terza struttura, uno strato mesoporoso di TiO_2 è stato aggiunto sullo strato di TiO_2 compatto per fornire una struttura di sostegno ai nanocristalli di Bi_2S_3. Infine, è stata testata un'architettura con uno strato mesoporoso di TiO_2 ricoperto da una soluzione di nanocristalli dispersi in P3HT. L'ultima architettura è risultata le più performante, mostrando una tensione di circuito aperto di 0.61 V, una densità di corrente di corto circuito di 1,05 mA/cm^2, un fill factor di 42,7% e un'efficienza di conversione di potenza dello 0.28%.

Gli esperimenti sul solfuro di rame (Cu_2S) hanno invece riguardato la procedura di sintesi e fabbricazione di film sottili. Abbiamo testato una nuova tecnica

per un processo di deposizione in fase liquida usando un sale metallico, acetato di rame(I) come sorgente di rame, tiourea come sorgente di zolfo e piridina come solvente. I precursori sono stati deposti via *spin coating* su diversi substrati, vetro ricoperto di FTO, TiO_2 compatto e TiO_2 mesoporoso, e i campioni sono stati caratterizzati otticamente con uno spettrofotometro.

Gli spettri di assorbimento dimostrano però che la tecnica attuale risulta in una fase mista di solfuro di rame non stechiometrico, e necessita di un'ottimizzazione per ottenere Cu_2S puro.

Estratto
Italian extract

Introduzione

La ricerca e lo sviluppo di soluzioni innovative nel campo del fotovoltaico è un campo in espansione a causa del crescente fabbisogno energetico e della necessità di una produzione sostenibile. Le attuali tecnologie basate sul silicio soffrono di alti costi e problemi di inquinamento, principalmente causati dai loro processi di produzione, motivi per i quali negli ultimi anni è costantemente cresciuto l'interesse in nuove soluzioni economiche ed ecologiche.

Questo lavoro riguarda l'uso di materiali *"green"* per applicazioni solari, che rappresentano un'efficace risposta al bisogno di un fotovoltaico efficiente, a basso costo ed eco-compatibile. In particolare sono stati svolti esperimenti su due materiali promettenti per queste applicazioni, il solfuro di bismuto (Bi_2S_3) e il solfuro di rame (Cu_2S).

Metodi

Solfuro di bismuto

Gli esperimenti riguardanti il primo materiale consistono nella progettazione dell'architettura del dispositivo. Sono state valutate le performance del materiale nelle seguenti strutture, schematizzate in figura 1:

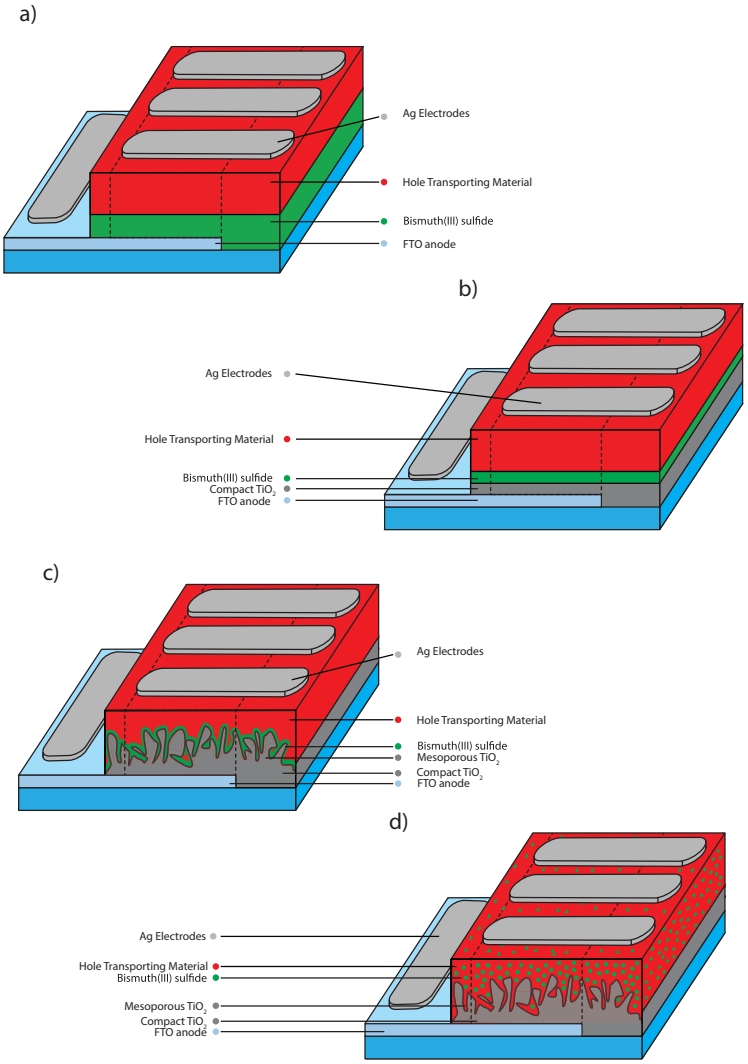

Figura 1: Immagine delle strutture testate con il Bi_2S_3.

- struttura planare FTO/Bi_2S_3/HTM

- struttura planare con uno strato blocca lacune di TiO_2: FTO/cp-TiO_2/Bi_2S_3/HTM

- struttura con uno strato mesoporoso di TiO_2: FTO/cp-TiO_2/mp-TiO_2/Bi_2S_3/HTM

- struttura con uno strato mesoporoso di TiO_2 e un *blend* di materiale trasporta-lacune e nanocristalli Bi_2S_3: FTO/cp-TiO_2/mp-TiO_2/Bi_2S_3:HTM

Con la prima struttura si vuole realizzare una semplice eterogiunzione planare. Il dispositivo è deposto su un substrato di vetro. L'elettrodo trasparente è costituito da FTO, su cui è deposto uno strato di ∼200 nm di Bi_2S_3 come assorbitore di luce e materiale di tipo n. In cima è deposto uno strato di ∼100 nm di un polimero con alta conducibilità di lacune (P3HT o spiro-OMeTAD a seconda degli esperimenti), su cui sono evaporati ∼100 nm di argento, che costituiscono i catodi del dispositivo.

La seconda struttura è simile alla prima, ma fra anodo e materiale attivo è aggiunto uno strato di ∼100 nm di TiO_2 compatto, la cui funzione è permettere il trasporto selettivo di elettroni, inibendo il passaggio di lacune.

La terza struttura ricalca l'architettura delle DSCs, differisce quindi dalle precedenti per l'aggiunta di uno strato mesoporoso di ∼300 nm di TiO_2, in modo da aumentare la superficie fra il solfuro di bismuto e lo strato di TiO_2, al fine di ottenere una migliore separazione della carica.

L'ultima struttura infine ricalca la struttura delle celle organiche, dove il *blend* non è però totalmente costituito da materiale organico, ma i nanocristalli di solfuro di bismuto sono miscelati al polimero.

Solfuro di rame

Il lavoro sul solfuro di rame consiste in esperimenti su una procedura di sintesi in-situ di questo materiale. La tecnica prevede la deposizione diretta da soluzione di solfuro di rame su diversi substrati e con diverse temperature di riscaldamento. I substrati sono scelti in vista di applicazioni fotovoltaico, così sono stati testati vetro ricoperto di FTO, TiO_2 compatto e TiO_2 mesoporoso.

I materiali sono deposti via *spin coating*. Nella nostra procedura un sale metallico, acetato di rame(I) è usato come fonte di rame, tiourea come fonte di zolfo e piridina come solvente.

Risultati

Solfuro di bismuto

In Figura 2 sono riportate le performance dei dispositivi realizzati con le prime tre architetture illustrate nella precedente sezione.

I dispositivi presentano efficienze estremamente basse, principalmente dovute alle basse fotocorrenti. I valori di tensione di circuito aperto sono anche loro

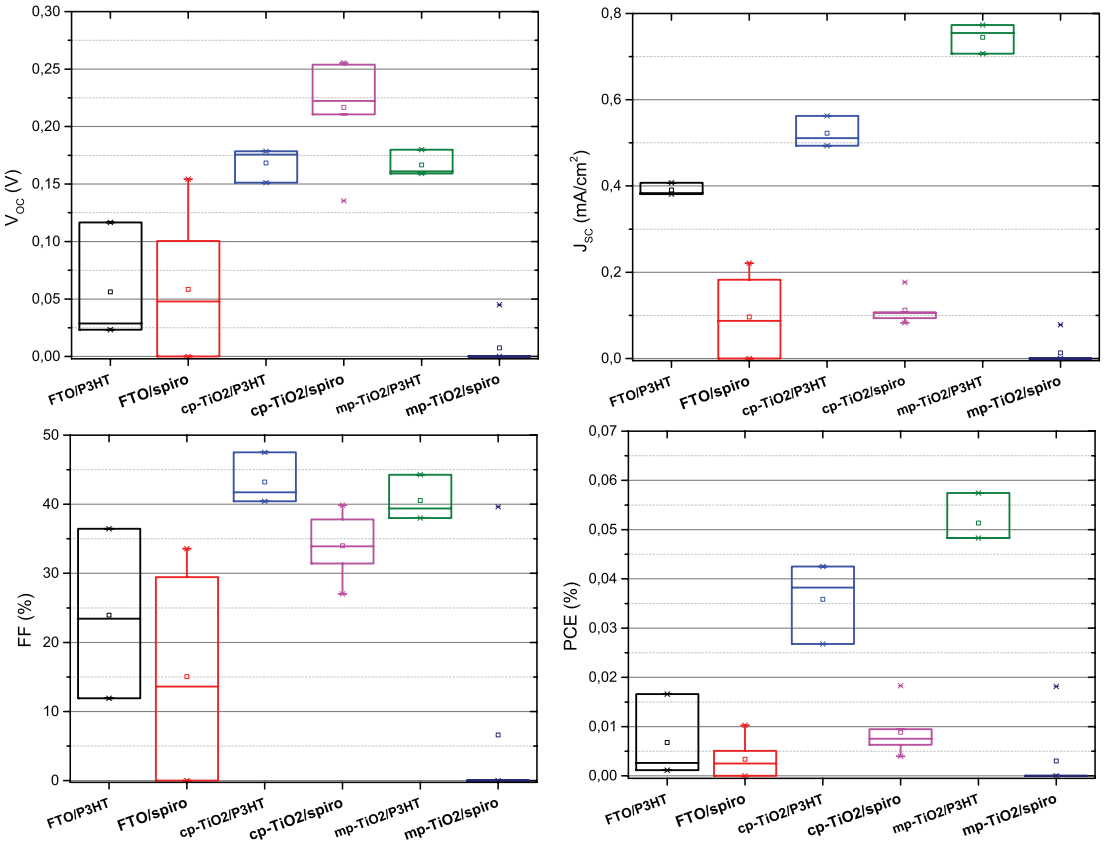

Figura 2: V_{oc}, J_{ss}, FF e PCE ottenuti nel primo esperimento con il solfuro di bismuto. Le etichette, da sinistra a destra, si riferiscono alle seguenti strutture; FTO/Bi_2S_3/P3HT, FTO/Bi_2S_3/spiro-OMeTAD, FTO/cp-TiO_2/Bi_2S_3/P3HT, FTO/cp-TiO_2/Bi_2S_3/spiro-OMeTAD, FTO/cp-TiO_2/mp-TiO_2/Bi_2S_3/P3HT, FTO/cp-TiO_2/mp-TiO_2/Bi_2S_3/spiro-OMeTAD.

lievemente inferiori a quanto è possibile trovare in letteratura, probabilmente a causa di alte ricombinazioni.

In Figura 3 sono riportati i risultati di un secondo esperimento identico al precedente, in cui però è stata utilizzata una soluzione di nanpoarticelle di Bi_2S_3 ottenuta da una sintesi ri-ottimizzata per ridurre i difetti superficiali.

Molti dispositivi risultano non funzionanti, ma i dispositivi che mostrano un'azione fotovoltaica presentano valori lievemente più performanti, in particolare per quanto riguarda i valori di tensione di circuito aperto (V_{oc}). Dall'analisi delle interfacce eseguite con microscopia elettronica a scansione illustrata nel lavoro è emerso che l'alto tasso di insuccesso potrebbe essere dovuto ad una distruzione dello strato di Bi_2S_3 durante la deposizione degli strati successivi.

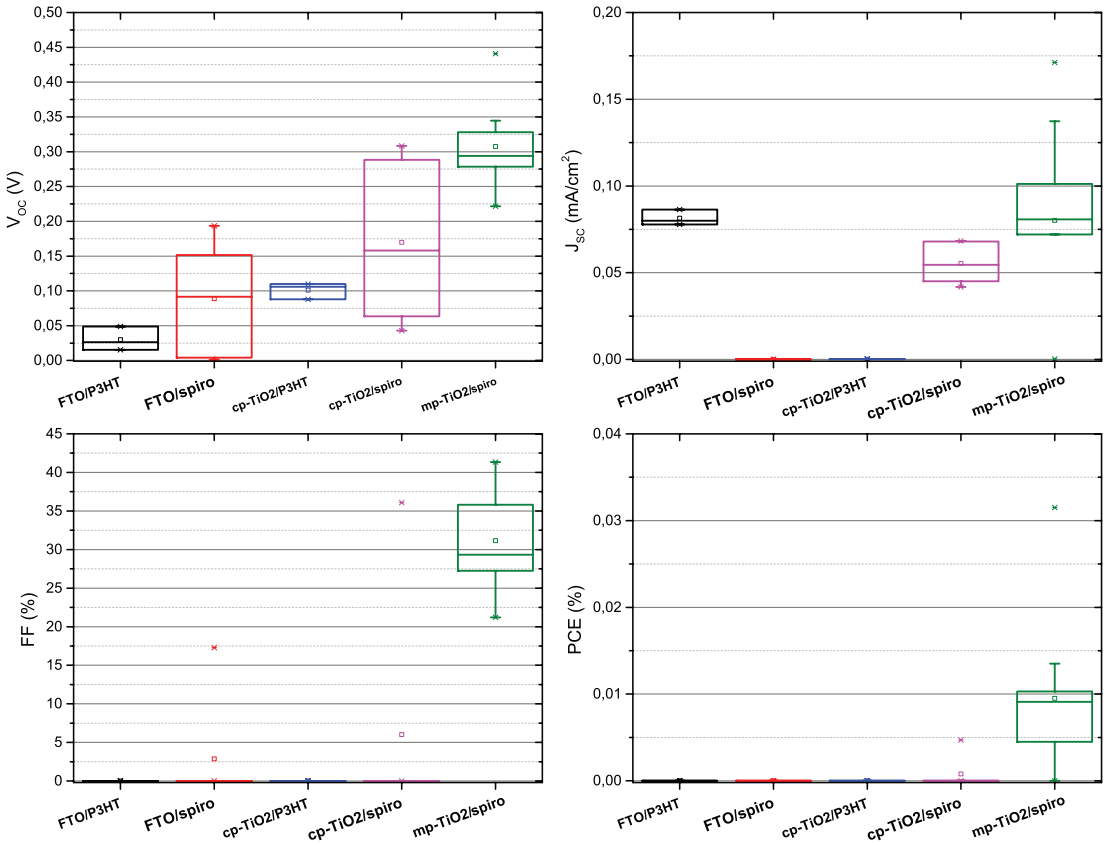

Figura 3: V_{oc}, J_{ss}, FF e PCE ottenuti nel secondo esperimento con il solfuro di bismuto. Le etichette, da sinistra a destra, si riferiscono alle seguenti strutture: FTO/Bi_2S_3/P3HT, FTO/Bi_2S_3/spiro-OMeTAD, FTO/cp-TiO_2/Bi_2S_3/P3HT, FTO/cp-TiO_2/Bi_2S_3/spiro-OMeTAD, FTO/cp-TiO_2/mp-TiO_2/Bi_2S_3/P3HT, FTO/cp-TiO_2/mp-TiO_2/Bi_2S_3/spiro-OMeTAD.

Il terzo esperimento (Figura 4) mostra le performance del dispositivo realizzato con la quarta struttura elencata nella precedente sezione, che dovrebbe permettere di superare i problemi di interfaccia riscontrati nei precedenti esperimenti. In Figura 4 sono riportate le prestazioni delle celle, in una struttura con 100 nm o 300 nm di strato mesoporoso di TiO_2, in cui è stato effettuato o meno il procedimento di scambio del legante che ricopre i nanocristalli (acido oleico) con una molecola più corta, al fine di migliorare le proprietà elettriche.

I dispositivi presentano valori di V_{oc} ben più alti dei precedenti e di quanto riscontrabile in letteratura per simili dispositivi, e sebbene i valori di J_{sc} risultano ancora bassi si ottiene globalmente un incremento di un ordine di grandezza della

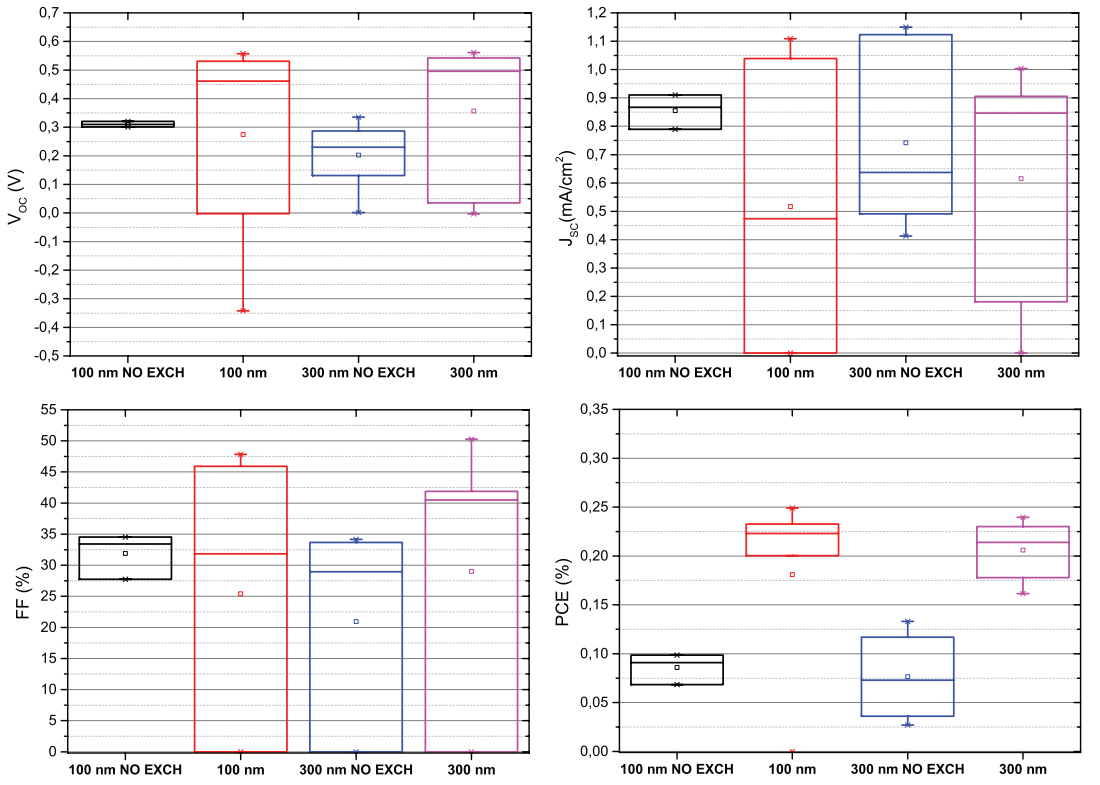

Figura 4: V_{oc}, J_{ss}, FF e PCE ottenuti nel secondo esperimento con il solfuro di bismuto. Tutti i campioni hanno la seguente struttura: FTO/cp-TiO_2/mp-TiO_2/Bi_2S_3/P3HT. lo spessore dello strato di mp-TiO_2 è 100 nm per le prime due colonne, 300 nm per le altre. Le etichette "NO EXCH" indicano i campioni non sottoposti al processo di scambio di legante.

PCE rispetto ai precedenti esperimenti. Il confronto fra i vari valori di PCE mostra inoltre l'effetto positivo del processo di scambio di legante.

Solfuro di rame

In figura 5 sono riportati gli spettri di assorbimento del Cu_XS deposto su FTO, su TiO_2 compatto e su TiO_2 mesoporoso.

Gli spettri di assorbimento del Cu_XS mostrano una sintesi che non ha prodotto Cu_2S stechiometrico, come evidenziato dal picco attorno 1050 nm, attribuibile ad una risonanza plasmonica superficiale[1], che risultarebbe soppresso in caso di materiale semiconduttivo. Un'ottimizzazione delle concentrazioni dei reagenti e delle procedure di deposizioni è quindi auspicabile per ottenere un prodotto semiconduttivo.

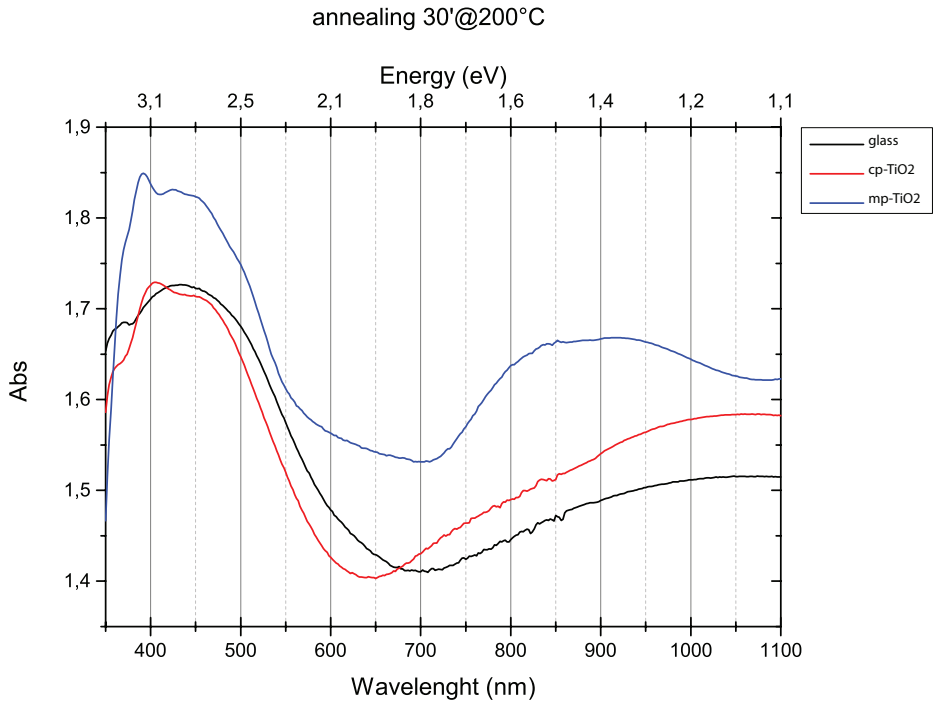

Figura 5: Confronto degli spettri di assorbimento di Cu_XS deposti su diversi substrati. G13 indica Cu_XS deposto su FTO, C8 è Cu_XS deposto su TiO_2 compatto e M16 è Cu_CS deposto su TiO_2 mesoporoso.

List of Abbreviations

BHJ bulk etherojunction

CB conduction band

CBD chemical bath deposition

CDCA chenodeoxycholic acid

CIGS copper indium gallium (di)selenide

DSCs dye-desitized solar cells

DOS density of states

EPBT energy pay-back time

FF fill factor

FTO SnO_2:F, fluorine-doped tin oxide

HOMO highest unoccupied molecular orbital

HTM hole transporting material

ITO indium tin oxide

$\mathbf{J_{SC}}$ short circuit current density

Li-TFSI bis(trifluoromethylsulfonyl)amine lithium salt

LUMO lowest occupied molecular orbital

MEG multiple electron generation

OPV organic photovoltaic

PCE power conversion efficiency

QD quantum dots

spiro-OMeTAD 2,2',7,7'-tetrakis(N,N'-di-p-methoxyphenylamine)-9,9'-spirobifluorene

ssDSCs solid state dye-sesitized Solar Cells

TCO transparent conductive oxide

VB valence band

$\mathbf{V_{OC}}$ open circuit voltage

Introduction

In 1850, when sir William Gladston, then British Chancellor of the Exchequer, asked of the practical value of electricity, Micheal Faraday answered "One day sir, you may tax it".

If in the 19th century the potentiality of electricity was not so clear, nowadays its role of main form of energy is so consolidated that in the common language the words electricity and energy are almost synonymous. Our society uses globally tens of PWh of energy every year and, despite major efforts towards improving the efficiency of energy consumption, this quantity is increasing.

This growth is highlighting a serious problem of energy supply, which is currently organized in a non sustainable way in the long term. According to the last report from International Energy Agency,[2] in 2011 more than 80% of energy supply came from fossil fuel (i.e. oil, coal or natural gas), a non renewable kind of source that will then run out.

It is then clear that a reorganization of energy supply is needed, and among the renewable sources, solar energy is regarded as the most available, as the energy falling on the earth's surface in 1 hour is more than all the energy consumed by humans in an entire year.[3]

For these reasons, research and development for innovative solutions in photovoltaics is a growing field. Over recent years has been increasing interest in new cheap and environmental friendly solutions capable to substitute current silicon-based technologies that suffer of high costs and pollution problems, which mainly derive from their production processes.

This thesis deals with the use of *"green"* materials for solar cells applications, that are a promising answer to the need of cheap, performing and eco-friendly photovoltaics. In the last couple of decades new devices based on a broad range of materials have been proposed and different ways have been followed in order to overtake conventional photovoltaics. This kind of devices differ not only in the materials but also in the device architecture, and different are the physical mechanisms governing the power generation.

This work is structured as follows:

In **Chapter 1** we will give an overview of the main existing technologies in the photovoltaic field. We will describe both the conventional solar cells, in which free carriers are the main photoexcited species, and solar cells based on exciton generation by light absorption. We will also give a brief description of the benchmark parameters used to compare device performances.

In **Chapter 2** we will presents the materials used in this work and will give a detailed description of the experimental methods we followed. In particular, we will describe the fabrication techniques of solar cells with bismuth sulfide and the synthesis procedure of copper sulfide.

Finally in **Chapter 3** and **Chapter 4** we will show a detailed analysis of the experimental results, and outlooks for future works will be presented.

CHAPTER 1

New generation green photovoltaic

1.1 Introduction

In this first chapter we will give an overview of the most promising technologies in which *"green"* materials can be used, dividing them by the main working principle on which the operations are based.

A first section will be dedicated to conventional solar cell devices, which are devices where light absorption causes a generation of free charge carriers. Among these devices we will focus on thin films solar cells and in particular copper indium gallium (di)selenide (CIGS) solar cells, the most performing solution of this category.

In the second section we will then review devices based on exciton generation by light absorption, and in particular full organic solar cells, dye-desitized solar cells (DSCs) and quantum dots (QD) cells.

In the last section we will finally summarize the main benchmark parameters, to give a quantitative meter to compare solar cells performance.

1.2 "Conventional" solar cells

Conventional solar cells are constituted by light-absorbing semiconducting material. Electronic properties of semiconductor can be obtained solving the time-independent Schrödinger equation for the electron:

$$\nabla^2\psi + \frac{2m^*}{\hbar}[E - U(\vec{r})]\psi = 0 \tag{1.1}$$

where ψ is the electron wave function, m^* is the effective mass of the electron, $\hbar$ is the normalized Planck constant, E is the energy of the electron and $U(\vec{r})$ is the periodical potential energy inside the semiconductor.

Its solutions define the band structure of the semiconductor, that are the allowed electron energies and the relationship between the electron's energy and momentum. In a simplified model we have two bands, the lowest valence band (VB), in which electrons are highly bounded to the semiconductor lattice, and the highest conduction band (CB), in which electrons have enough energy to move through the semiconductor. VB and CB are divided by an energy gap of non allowed energy states.

Electrons will occupy an energy state E following the Fermi-Dirac distribution

$$f(E) = \frac{1}{e^{(E-E_f)/kT} + 1} \tag{1.2}$$

where E_f is the Fermi level, that can be defined as that energy level of an electron such that at equilibrium it has a 0.5 probability to be occupied at any time, k is Boltzmann's constant and T is the absolute temperature.

If we introduce electron-donor (and we will talk of n-doped material) or electron-acceptor (p-doped material) impurities, we will increase the electron densities (and then electron conductibility) in the CB of the n-material and holes densities (and holes conductibility) in the VB of the p-material, causing a downward shift of the Fermi level respects to the bands for the p-material and an upward shift for the n-material.

When a p-semiconductor and a n-semiconductor are brought in contact we observe a band bending at the junction, and this induces a built-in voltage given by

$$\phi_{bi} = \frac{kT}{q} \ln\left(\frac{N_a N_d}{n_i^2}\right) \tag{1.3}$$

where n_i is the number of electrons in the conduction band in an intrinsic semiconductor and N_a and N_d are the densities of acceptor and donor impurities.

A schematic picture of the band structure is represented in Figure 1.1,

When light impinges into the junction, photons can pass through the film, can be reflected or can be absorbed as described by the Lambert-Beer law for the light intensity:

$$I(x) = I(0)(1 - R(E))e^{-\alpha(E)x} \tag{1.4}$$

where $\alpha(E)$ is the absorption coefficient and $R(E)$ is the surface reflectivity.

Absorbed photons cause a promotion of electrons to the CB leaving a hole in the VB.

Photo-generated carriers are of orders of magnitude less than majority carriers already present due to doping. Consequently light absorption does not alter significantly the number of majority carriers but photo-generated minority carriers outweighs minority carriers existing in the doped solar cell in the dark, so minority carriers in an illuminated solar cell can be approximated by the number of light generated carriers.

Due to the high dielectric constant of a semiconductor material, the bounding Colombian forces are easily overcame by thermal energy, thus, free charges are the primary photoexitations.

Minority carriers diffuse through the device and, if they do not recombine, they can reach the charge depletion region where the built-in electric field will cause a drift current that will overtake the diffusion current.

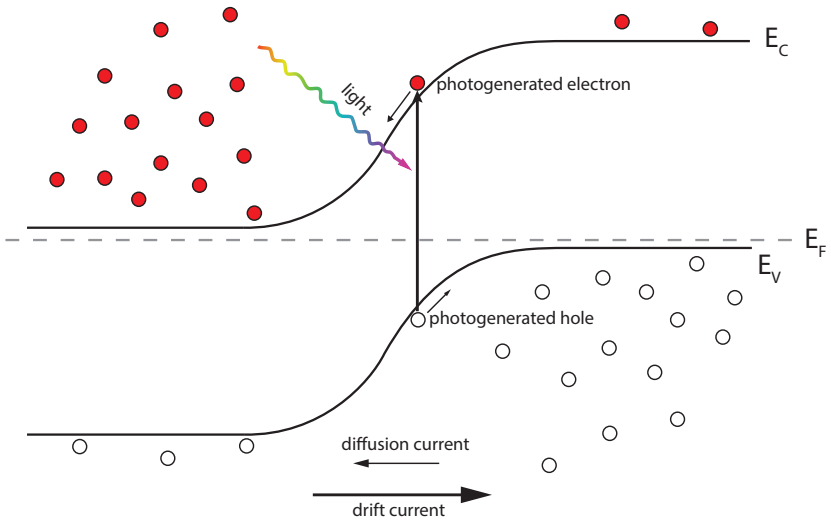

Figure 1.1: Schematic band diagram of a conventional solar cell. Red circles represents electrons and white circles represent holes. When light comes to the device it can cause a pair photogeneration. If photogenerated carriers reach the charge depletion layer (i.e. the band bended region) they will experience the built-in electric field resulting in a drift current.

Recombination occurs mainly trough four effects:

- **Shockley-Read Hall recombination**, caused by trap states that act as

recombination sites. For a p-type semiconductor, in low injection condition ($n_0 \leq n \ll p_0$) the recombination rate is given by

$$U_{\mathrm{SRH}} \approx (n - n_0)/\tau_n \tag{1.5}$$

where $\tau_n = (B_n N_t)^{-1}$ is the electron lifetime, N_t is the trap states density with energy E_n, $B_n = v_n \sigma_n$, where v_n is the thermal velocity of the electrons and σ_n is the capture cross section;

- **radiative recombination**, that is simply the inverse of optical generation process, and its rate (in a p-material) is given by

$$U_{\mathrm{rad}} \approx (n - n_0)/\tau_{\mathrm{rad}} \tag{1.6}$$

where $\tau_{\mathrm{rad}} = (B_{\mathrm{rad}} N_{\mathrm{a}})^{-1}$ is the radiative electron lifetime and B_{rad} is the radiative recombination coefficient;

- **surface recombination**, due to high defects concentration at the surface or at the interface of an etherojunction. Carriers recombination over time in a p-material is given by

$$U_s = S_n(n_s - n_0) \tag{1.7}$$

where S_n is the effective recombination velocities;

- **auger recombination**, where an electron-hole recombination promotes a secondary electron to a higher energy level in the conduction band.

Analogous equations can be written for the n-type materials.

We can see that all recombination effect are dependent on the minority carrier concentration only, because they are the limiting carrier in the recombination process.

Conventional solar cells are made of silicon. Considering that this is an indirect gap material the thickness of the device must be > 700 μm in order to absorb enough light. This is a not desirable value for commercial production because the wafer cost for a thick material can be very high, mainly because silicon is obtained from a high-expensive purification procedure from SiO_2. Moreover collection of photo-generated carriers will be small because it is difficult to have a minority-carrier diffusion length comparable with this thickness.

With some expedience the thickness can be reduced, but silicon cells still have high production cost and long energy pay-back time (EPBT). This is why many research branches focused on new materials to be used in a thin film configuration and capable to reduce cost production and EPBT.

1.2.1 Thin Films: Copper Indium Gallium (di)selenide (CIGS)

Thin films solar cells offer the possibility to reduce the amount of material used for the device fabrication. The drawbacks of the thickness reduction is obviously the reduced absorbed light, as show in equation 1.4. New materials are then needed to overtake this problem and to make possible high light absorption with thickness of few micrometers. One of the most promising and performing materials is the copper indium gallium (di)selenide.

The history of CIGS solar cells starts with the work done at Bell Laboratories in the early 1970s, were a first $CuInSe_2$ photo-detector were made by evaporating n-type CdS onto p-type single crystals of $CuInSe_2$.[4] Optimization for solar cells from Shay et al. allowed to obtain a power conversion efficiency (PCE) of 12% as - they wrote in their work - "*measured on a clear day in New Jersey*".[5]

This kind of devices were then studied during the 1980s by Boeing, which tried to solve difficult manufacturing issues related to yield, scale-up, and throughput implementing many advancements mainly focused on deposing $Cu(InGa)Se_2$ by coevaporation.

The main potential of CIGS is the possibility of accommodating large variations in composition of (Ga)/(In+Ga) ratio without appreciable differences in optoelectronic properties, which, along with absence of polluting elements, made it a good material for efficient "low-cost" PV modules.

$CuIn_{1-x}Ga_xSe_2$ has an energy gap of[6]

$$E_g = 1.010 + 0.626x - 0.167x(1-x) \tag{1.8}$$

and an absorption coefficient of more than 10^5 cm^{-1} for photons of higher energy than 1.5 eV.[7] For solar cells a typical value of x is $\sim 0.2 \div 0.3$.

$CuInSe_2$ with an excess of Cu is always p-type, but In-rich films can be made p-type or n-type. If annealed in a selenium overpressure, n-type material can be converted to p-type because Se vacancies, V_{Se}, act as compensating donors in p-type films. $Cu(InGa)Se_2$ films for devices are grown with the excess of Se

to obtain p-type films with a carrier concentration of about $10^{16}cm^{-3}$. There is a large spread of values for holes mobility. The highest is obtained for epitaxial films, where 200 $cm^2/V{\cdot}s$ has been measured with a $10^{17}cm^{-3}$ hole concentration[8]. For polycristalline p-type films used in devices the mobility value range from 5 to 50 $cm^2/V{\cdot}s$, but this values are probably limited by transport across grain boundaries.

From theoretical calculation it is possible to have the energy of defects considered most important for devices, shown in 1.1.[9]

Defect	Energy position	Type
V_{Cu}	$E_V + 0.03$ eV	Shallow acceptor
In_{Cu}	$E_C - 0.25$ eV	Compensating donor
V_{Se}		Compensating donor
Cu_{In}	$E_V + 0.29$ eV	Recombination center

Table 1.1: Most important intrinsic defects for device-quality $CuInSe_2$

The most promising deposition method for the commercial manufacture are vacuum coevaporation and two step processes. In the first all constituents, Cu, In, Ga, and Se are simultaneously evaporated from elemental sources at temperature greater than 1000 ℃ on a substrate heated from 400 to 600 ℃ and the $Cu(InGa)Se_2$ film is formed in a single growth process. In the second approach Cu, Ga and In are deposed using low-cost and low-temperature methods (electrodeposition, electron beam evaporation, screenprinting), then the films are annealed in a Se atmosphere a 400 to 600 ℃.

A typical device structure is shown in Figure 1.2. The back contact is made of molybdenum, typically deposed by direct current sputtering.

The etherojunction is made with a thin film of n-type CdS, usually deposed via chemical bath deposition (CBD). The cadmium content in CIGS PV modules is very low, but it would preferable to eliminate cadmium in new products, either finding another n-type material that replaces CdS or omitting it using the overlaying buffer layer of ZnO as n-tye layer. Successful replacements have been made with ZnS[10], $ZnIn_xSe_y$[11] or $In_x(OH,S)_y$[12].

The buffer layer of undoped high-resistivity (HR) Zinc Oxide (ZnO) is deposed by radio frequency (RF) magnetron sputtering from an oxide target. The role of ZnO layer results from locally non-uniform electronic quality of the CIGS layer that can be modeled by a parallel diode with high recombination current, whose effects are reduced by the series resistance of the HR ZnO layer[13]. Another

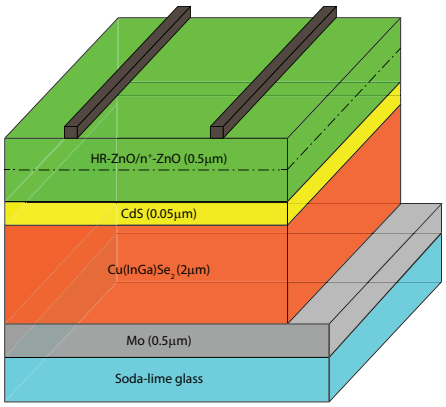

Figure 1.2: Schematic cross section of a typical $Cu(InGa)Se_2$ solar cell.

explanation is given considering possible pinholes in the thin CdS layer, that would be resolved by the ZnO layer.

Another function of the HR ZnO buffer layer is to add protection of the interface from sputter damage during the front contact deposition.

The top electrode is made of a transparent conductive oxide (TCO), usually ZnO:Al (AZO) deposed by RF magnetron sputtering.

A band diagram of the resulting device is shown in Figure 1.3

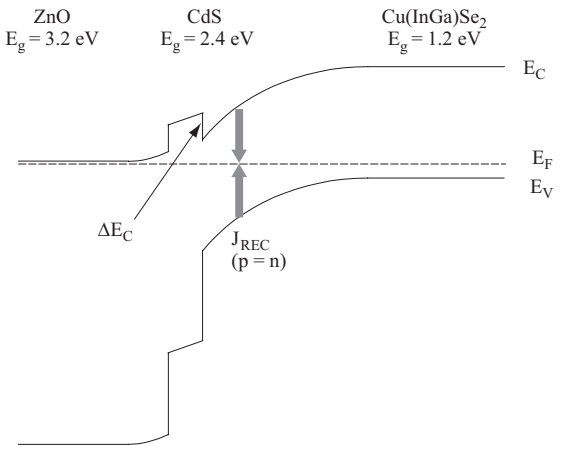

Figure 1.3: Band diagram of a $ZnO/CdS/Cu(InGa)Se_2$ device at 0 V in the dark. Reproduced from [14].

1.3 Excitonic Solar Cells

In the previous section we described devices in which light absorption cause a free electron-hole pair generation. To have absorption, photons needs to have energy equal or higher than the energy band gap, with an electrical band gap equal to the optical band gap. In specific materials, light absorption results in the production of correlated charge pair excitations that cannot thermally dissociate in the chemical phase where is formed due to their binding energy $\gg kT$. This excited states can be described as a quasi-particle (called exciton) constituted by an electron and an electron hole bounded by the electrostatic Coulomb force. In this case, optical band gap is not equal to electric band gap because absorption, due to the Coulombic binding energy to be considered in the energy balance, occurs also at energies lower than electrical band gap.

In order to obtain free charge carriers the photo generated excitons must undergo a dissociation process of the bound electron/hole couple. This process has to compete with exciton relaxation that can occur via many processes summarized in the Jablonski diagram of Figure 1.4 The non radiative processes are internal

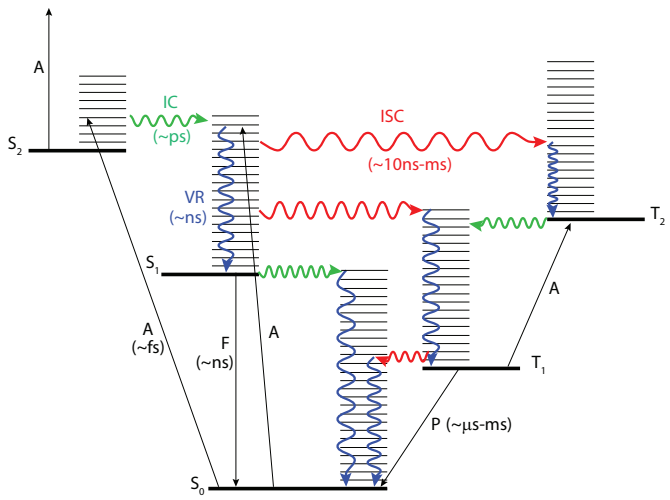

Figure 1.4: Jablosnki diagram in the optically excited molecule. IC: internal conversion; ISC: intersistem crossing; VR: vibrational relaxation, A: absorption, F: fluorescence; P: phosphorescence. Adapted from [15]

conversion (IC), that is the transition between states of same spin multiplicity, intersystem crossing (ISC) that is the transition between different spin manifolds, and vibrational relaxation (VR), that is the process of redistribution of vibrational energy from optically coupled modes to "dark" modes.

Radiative processes are absorption, fluorescence and phosphorescence. In Figure 1.4 are also reported the typical time scales.

Charge photogeneration can occur via autoionization. In this process absorption of photons with energy greater than the energy gap cause the generation of a neutral singles state S_n; auto-ionization (AI) cause a generation of hot carrier pair, which may thermalize and generate an intermediate, bound charge pair, referred to as Charge Transfer state (CT). This is a weakly-bounded excited state that can be easily ionized and is considered as precursor of charge carriers. Charge separation then occurs. A picture of the process is represented in Figure 1.5. The

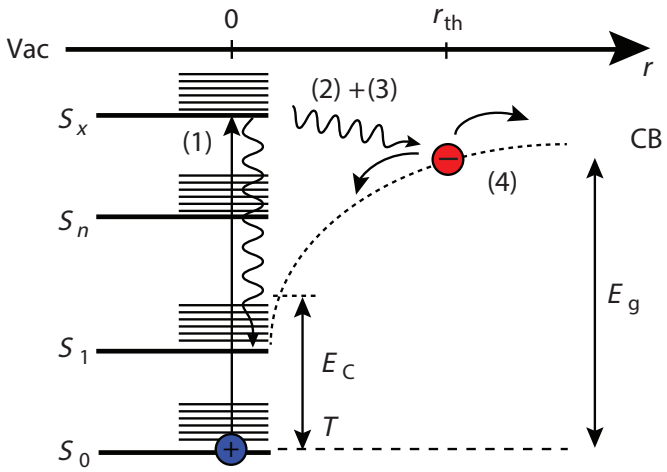

Figure 1.5: Multistep charge photogeneration process. (1)Photon absorption and generation of a neutral singlet state S_n, (2) Auto-ionization with generation of hot carrier pair; (3) Thermalization and generation of an intermediate, bound charge pair; (4) Dissociation of the intermediate pair into free carriers. Adapted from [15]

process described above is highly inefficient in materials used for excitonic solar cells. To obtain charge dissociation it is possible to create an heterojunction between two different materials. Recalling conventional photovoltaics nomenclature, these two materials are generally referred to as n-type (or electron-acceptor or electron-conducting) and p-type (or electron-donor or hole conducting) materials.

The energy levels of the two materials are engineered so that difference between LUMO levels of the electron-acceptor and the electron-donor is more than ionization energy. So if exciton is near the interface, electron injection to the acceptor molecule will be energetically favoured and will occur with large probability. This process implies the localization of exciton at the interface. Excitons located away from the interface cannot dissociate efficiently, but energy can propagate

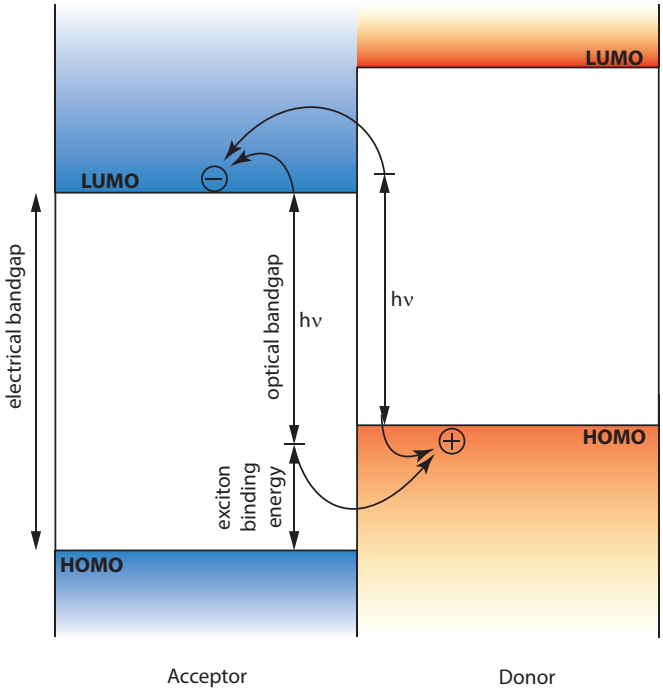

Figure 1.6: Schematic picture of the donor acceptor interface. HOMO-LUMO gap is more than exciton binding energy, and career separation is energetically favoured.

through the material "jumping" from one site to another. Energy migration, that is the energy transport between molecules of the same species, or energy transfer, occurring between molecules of different species, can occur by radiative process, involving the emission of a photon by the donor molecule and subsequent absorption by the acceptor molecule, or can be radiationless. The former can be described by two models: Förster dipole coupling and Dexter electron exchange models for energy transfer. The first is a migration process described in terms of interaction of transition dipole moments of the donor and acceptor molecules and it has a rate of[15]

$$k_{DA} = \frac{1}{\tau_D}\left(\frac{R_0}{R}\right)^6 \tag{1.9}$$

where τ_D is the excited-state lifetime of the donor and R_0 is the critical transfer distance at which the energy transfer rate is equal to the deactivation rate of the isolated molecules.

Dexter model extend Förster analysis to a higher multipole-multipole and electron-exchange interaction. In close distance interactions, quadrupole and higher terms in the multipole expansion are relevant, and an electron-exchange interac-

tion occurs. Transition rate is given by[15]

$$k_{DA}(\text{exchange}) = Be^{-2\frac{R_{DA}}{L}}J \tag{1.10}$$

where B is a coupling constant, R_{DA} is the donor-acceptor distance and J is the spectral overlap integral. These energy transfer mechanisms are needed to collect charge from excited states originated far from D/A interfaces, but are very inefficient compared to free charge moving in conventional semiconductor.

In the following sections we will analyse excitonic solar cells operations to understand how phenomena described above can be used for power generation.

1.3.1 Organic Photovoltaic

Organic materials, whose name come from the 1st century belief that they could be synthesised by living organisms only, are conventionally those compounds rich in carbon with an oxidation number less than +4. Carbonium has six electrons,

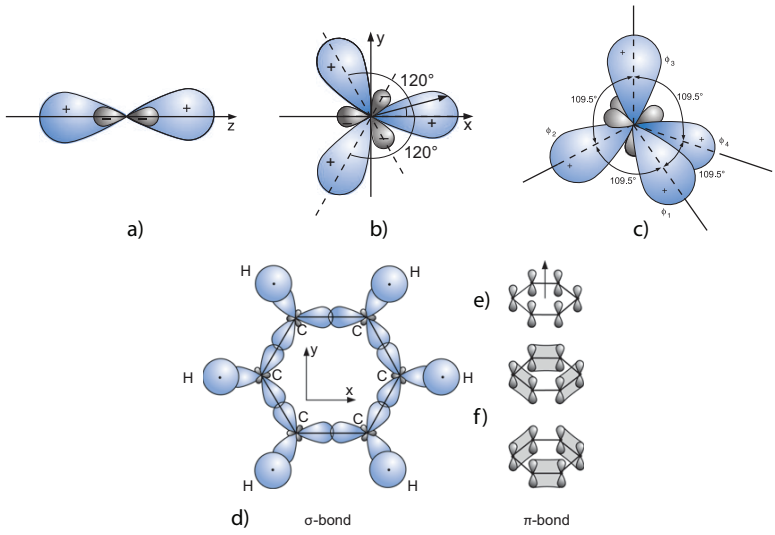

Figure 1.7: Picture of hybrid orbitals. a) sp hybridization b) sp^2 hybridization c) sp^3 hybridization d) σ-type molecular orbitals in benzene formed with sp^2-hybrid atomic orbital from the C atoms e) π-type orbitals, f) two indistinguishable π-type orbital configurations. Adapted from [16]

and its electronic configuration is $1s\ 2s^2 2p^2$. Depending on the structural and electronic configuration of the molecule in which carbon exists, many electrons can interact so that atomic orbitals given by the solution of the Shröedinger equation for an hydrogenic atom are no more eigenstates, and electronic configuration needs

to be described by a linear combination of conventional orbitals also known as *hybrid orbitals*.

Possible hybrid orbitals are given by the linear combination of the 2s orbital with one of the three p orbitals, and we talk of sp hybrids; a combination of 2s orbital with two of the 2p orbitals gives the sp^2 hybrid and combination of orbitals 2s whit all three 2p orbitals gives the sp^3 hybridation. A graphical representation of hybrid orbitals is given in Figure 1.7.

When molecules with sp^2 or sp hybridization of the carbon atoms interact, the hybridized orbitals between adjacent carbon atoms form strong and localized covalent bonds referred to as σ bonds, while non hybridized p orbitals combine forming weaker π-bonds with electric charge delocalized in the molecular plane.

If several carbon atoms are connected together, electrons of the p atomic orbitals are delocalized inside the band of states created by π-bonds, while σ electrons will be on the axis connecting the carbons nuclei. The resulting chain is not composed of equally spaced carbon atoms because this kind of structure results unstable, as demonstrated by Frölich[17] and Perierls[18] in the 1930s. The stable configuration is composed by atoms close in couples, with an alternation of single and double covalent bonding between two adjacent carbon atoms. This configuration is called π-*conjugation*. Molecular orbitals are still delocalizated along the chain, but electron cloud is denser along double covalent bonding, where the interatomic distance is shorter. Considering the energy of the system in the momentum spaces, the resulting dispersion diagram of this structure (Figure 1.8) show a gap at $k=\pm\pi/2a$, where a is the lattice constant of the chain. This result in a semiconductive behaviour of conjugated molecules.

When we consider molecular solid of organic materials, solid state aggregation is driven by the Van der Waals forces, whose formation energy is much lower than a covalent bond. Interaction between molecules is then weak, so this kind of materials have high mechanical flexibility, but on the other hand the delocalization of the electric charge is not extended to the whole solid, so electrical properties are poor compared to inorganic semiconductors.

Charge transport is then limited by trap states caused by the localization of wave functions over one or few molecules. When trapped in local states, charge carriers can polarize locally the surrounding environment modifying the molecular structure. The coupling between electron and a local deformation can be described as an electron-phonon coupling, and this couple can be seen as a charge carrier called *polaron*. The polaron create a new energetic state in the HOMO-LUMO

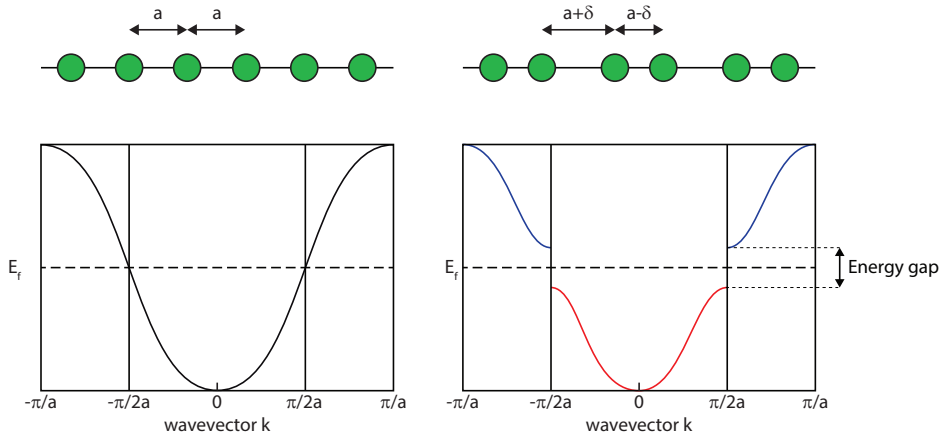

Figure 1.8: Dispersion diagram of a chain of equal spaced carbon atoms (left) and of a chain of atoms close in couples (right). The alternation of single covalent bonding (longer interatomic distance) and double covalent bonding (smaller interatomic distance) results in a gap at k=$\pm\pi/2a$.

gap, and carriers can move via *hopping* between adjacent states.

Activities on this class of materials were established during the late 1970s and early 1980s, and they had been immediately recognized as a potential low cost approach to large area solar cells. First devices based on conduction polymers (mainly polyacetylene) had a very poor efficiency.

With the first generation of highly soluble polymer semiconductors (including polythiophenes (PT) and polyphenylenevinylenes (PPV)) the situation began to improve, but quality, reproducibility and purity of these polymers at that time was too low for devices fabrication. However the main reason for low efficiency was evident when first studies about photoexcited states in organic semiconductors started to explain mechanism of charge generation. Detailed studies of this materials indicated that only a small fraction of excitons dissociate in a simple OPV device, and the separation of these excitons was found to be driven by the presence of defects or impurities.[19] Research focused then to identify mechanism of charge separation. In 1992 the first donor/acceptor interface was realized using the fullerene C60 deposited by vacuum sublimation onto the polymeric donor.[20]

A major breakthrough was the observation that mixing the donor and acceptor materials together forming distributed interfaces led to a higher efficiency. This arose from the fact that exciton length in organic semiconductor is of the order of 10 nm, so in planar device (with a ∼100nm usual thickness) most of photogenerated excitons decay before reaching the interface. In 1991 Yu et al.[21] realized the first solution processed bulk etherojunction (BHJ) cell using a highly soluble

fullerene derivative, phenyl-C61-butyric acid methyl ester (PCBM), to achieve sufficient percolation of charges through both components. This device reached PCE under monochromatic light of 2-3% (AM 1.5 efficiency was not measured, it can be estimated to be low than 1%).

Research on controlling the morphology of the donor-acceptor interfaces has been one of the dominating research branch in OPV, but nowadays there is still no full consensus on how the ideal morphology should be. A fine dispersion of the acceptor in the donor material will lead to efficient exciton dissociation but poor charge transport, which would achieve an ideal optimum in a bilayer stack. On the other hand, charge generation happens only at the D/A interface, so the bilayer stack is inefficient for this process. Simulations[22] showed that the a "comb structure", with a domains width of 2 times the exciton diffusion length (see Figure 1.9) would achieve ideal performances, with a good charge transport and efficient exciton dissociation. The real bulk-heterojunction is also shown in Figure

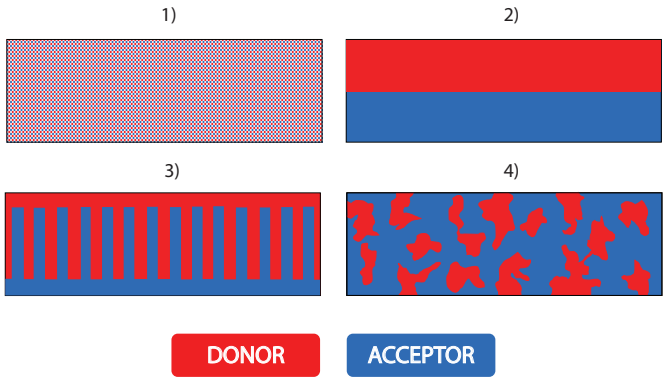

Figure 1.9: Schematic cross-section of nanomorphologies of bulk heterojunction solar cells. (1) Fine dispersion acceptor and donor materials, (2) bilayer stack, (3) ideal "comb" morphology of a bulk heterojunction solar cells and (4) typical real morphology of a solution processed device.

1.9. Connected domains with a typical size of tens of nanometers are formed in the film. Interfacial area optimization is optimized with several methods. For some materials additional thermal treatment of the active layer was found to be beneficial[23], and also the proper selection of processing solvents or the use of processing additives[24] (e.g. diiodooctane or dithiols) resulted in improved D/A interfaces.

Often BHJ cells are built on a transparent substrate coated with an indium tin oxide (ITO) layer. In the so called standard configuration (see Figure 1.10) the ITO is coated with a hole transporting layer (HTL). Thin films of doped con-

jugated polymer like PEDOT:PSS (poly(3,4-ethylenedioxythiophene)poly (styrenesulfonate)) or a thin oxide layer (e.g. MoO3) have been used as HTLs. On top of the HTL the photoactivelayer, a blend of donor and acceptor material is coated followed by an optional electron transport layer (ETL) and a low work function electrode. ETL materials are often oxides like ZnO or TiO_2. In the standard architecture, the top electrode is the cathode and calcium, barium or aluminium are applied for collecting the electrons generated in the photoactive layer.[25]

In the inverted architecture the transparent electrode coated on the substrate acts as a cathode. Either by modifying the work function of the electrode material, by applying an interfacial layer or by using transparent oxides like ZnO or TiO_2 a selective contact to the acceptor material in the active layer is formed. On top of the active layer a HTL like PEDOT:PSS or a thin oxide layer (e.g. MoO3) has been used and the device is finalized with an air stable high work function electrode material like silver or gold.[25] Both device architectures allow

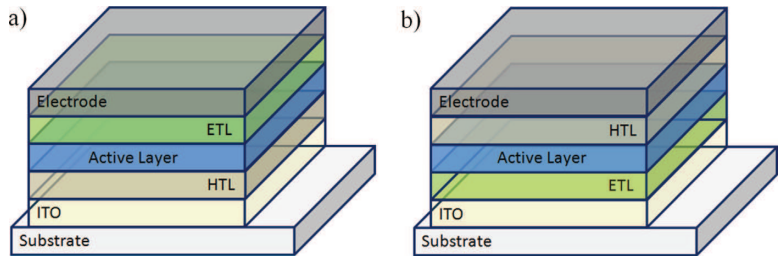

Figure 1.10: Different device architectures of bulk heterojunction solar cells. (a) Standard device design with the cathode on top of the device stack and (b) inverted device architecture with the cathode located on the transparent substrate. Reproduced from [25]

the preparation of high performance bulk heterojunction solar cells. The inverted design offers processing advantages (no vacuum process is required) and shows improved ambient stability due to the absence of a low work function electrode.[25]

OPV reaches efficiency of single solar cells of ∼10%, but actual devices suffer of high degradation problems. Mechanical and temperature stress can cause delamination, electrode failure or diffusion between layers, but the predominant degradation pathway in organic solar cells is the sensitivity of active layer to oxygen, which cause photochemical oxidation of interfaces. Devices can reach nowadays >5000 hours lifetime for encapsulated devices, that is a value good enough for first consumer applications, but improvement are needed to increase this value and increase commercial interest.

1.3.2 Dye Sensitized Solar Cells (DSCs)

DSCs are devices constituted by a light absorbing dye molecule, which has the solely function to absorb light, and two carrier transport materials so that light absorption and carrier transport occurs in two different media.

The work on sensitization of wide band gap semiconductors by adsorbed monolayer of dye molecules began in the 1970s. A first device was made by Tributsch et al.[26] with a chlorophyll sensitized ZnO electrode. This was the first example of photon to electric current conversion by charge injection of excited dye molecules into a wide band gap semiconductors. Other examples of sensitized devices were made in the following years,[27,28,29] but they obtained a poor efficiency, mainly because a monolayer of dye molecules on a flat surface can only absorb a very small fraction of the incident light ($\sim$1%).

A big improvement was obtained in 1991 when Grätzel and co-workers published their work[30] on DSCs based on a high surface electrode. The use of a mesoporous sintered film of $\sim$15 nm nanocrystalline TiO_2 particles allowed to increase of about 100 times the effective surface area per micrometer thickness compared with a flat film.

In a typical device structure the mesoporous metal oxide electrode (usually TiO_2) coated upon transparent conduction glass (usually SnO_2:F, fluorine-doped tin oxide (FTO)) is sensitized with a monolayer of dye molecules and filled with an iodide/triiodide based electrolyte. The devices is then capped with a counter electrode, as seen in Figure 1.11.

In the following years, in order to solve solvent leakage and corrosion from the ioddide/triiodide redox couple problems, Bach et al.[32] proposed a new device using an organic hole-trasporter, 2,2',7,7'-tetrakis(N,N'-di-p-methoxyphenylamine)-9,9'-spirobifluorene (spiro-OMeTAD), to replace the liquid electrolite realizing then fully electronic solid state dye-sesitized Solar Cells (ssDSCs).

In a DSC light is absorbed by the dye molecule which injects an electron from its excited state into the TiO_2 CB. The dye has the only function to absorb light so many materials are suitable beacuse there is no need of exciton diffusion, which is immediately located at the interface. The most commonly used are ruthenium complexes, but also squaraines, porphyrins, perylenes, pentacene cyanines or coumarin have been used.

The critical issue is achieving rapid electron injection into the TiO_2 to compete with intrinsic relaxation processes and sufficiently fast dye regeneration to com-

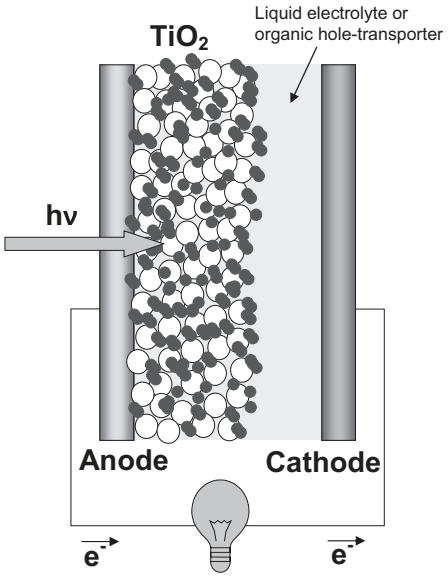

Figure 1.11: Schematic representation of a liquid Dye Sensitized Solar Cell. Reproduced from [31]

pete with interception (Figure 1.12, process 3). In the liquid-electrolyte DSC it strongly depends upon potential in the TiO_2. Systems with the lowest occupied molecular orbital (LUMO) energy levels located close to the TiO_2 and highest unoccupied molecular orbital (HOMO) far from the surface are of great utility for this issue. The oxidized photosensitizer accepts electron from the I^- ion redox mediator leading to regeneration of the ground state, and the I^- is oxidized giving I_3^-. Once regeneration of the dye has occurred, the charge recombination is very slow (tens of milliseconds to seconds). This is thought to be due to an intermediate ionic specie formed during dye regeneration, $I_2^{\bullet -}$, which can not recombine directly with electrons. The oxidized redox mediator, I_3^- diffuse toward the counter electrode and then it is reduced to I^- ions.

In the solid-state system, hole transfer from the oxidized state is on the nanosecond timescale, significantly faster than interception. Recombination of electrons from TiO_2 with holes in the HTM is instead much faster than liquid systems (micro- to milliseconds),[33] so this is a very intensively investigated process in DSCs operations, and interface engineering to reduce recombination is one of the most critical points to improve device performances.

Electrons injected in the mesoporous TiO_2 are then transported to the electrode. The mechanism for electron transport is still a debated topic, but there is much evidence that electron transport is governed by a detrapping of elec-

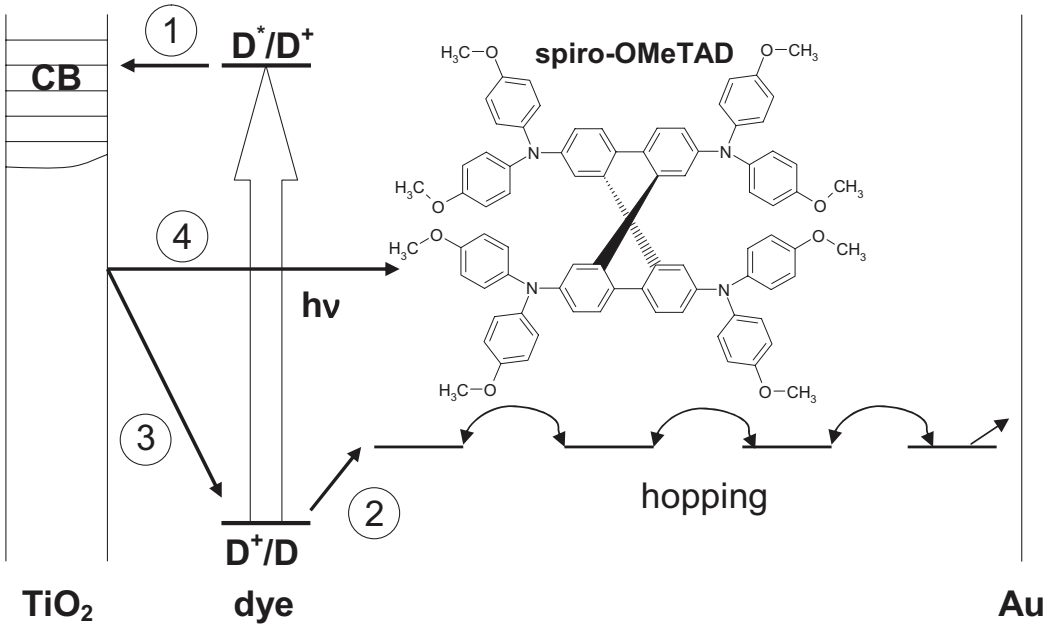

Figure 1.12: Schematic energy diagram for the electronic processes and main loss mechanisms in the solid-state dye-sensitized solar cell. Process 1: Electron injection from the excited state of the dye into the conduction band of TiO_2 (in the femtosecond range)[34,35]; Process 2: Hole transfer from the oxidized dye to the organic hole-transporter (between 0.3-1 ns)[36]; Process 3: Competition with recapture of injected electrons by the oxidized dye (few hundred microseconds)[37]; Process 4: Recombination of electrons in the TiO_2 and holes in the hole-transporter (micro- to milliseconds)[33]. For the liquid-electrolyte-based DSC the equivalent rates for the dye regeneration (2) and the charge recombination (4) differ significantly, with process 2 in the 10 μs range and process 4 in the millisecond to second time domain. Also shown is the chemical structure of spiro-OMeTAD, a hole transporter often employed in the solid-state DSCs. Reproduced from [31]

tron from sub-band gap states, deep in the tail of the density of states (DOS) to the CB, consistent with the multiple trapping-deptrapping model for charge transport.[38,39]

A post-deposition treatment of the TiO_2 in $TiCl_4$ aqueous solution has been demonstrated to improve photocurrent.[40] The role of $TiCl_4$ treatment is still debated, but the improvement of performance can be attributed to an increase of specific binding sites for dye absorption, a reduction of the TiO_2 surface area inaccessible for the dye[41] and to a reduced recombination rate.[42]

For the solid-state DSC a compact TiO_2 layer between the mesoporous layer and the FTO deposed via spray-pyrolysis deposition is used as a hole-blocking layer and to prevent current leakage.

Hole transport through the organic hole transport material spiro-OMeTAD occurs via polaron hopping between sites. The pristine material has an hole mobility

of about 10^{-4} V $^{-1}$s^{-1}. Ionic additives, bis(trifluoromethylsulfonyl)amine lithium salt (Li-TFSI), are usually added to obtain a p-doping of the material, which is accomplished by oxidation of the spiro-OMeTAD,[43] and values for hole-mobility are estimated to reach $\sim 10^{-3}$ V $^{-1}$s^{-1}.[43]

ssDSCs are less efficient than liquid ones, and one of the reason has been thought to be the relatively low charge mobility through the spiro-OMeTAD. Several hole transporting materials with higher mobilities have been tried with no gains. It has also been observed that electron conductivity through the mesoporous TiO_2 is lower than the spiro-OMeTAD, so it can not be the limiting factor. In fact, it has been observed that infiltration of the hole transporting material is the critical point to obtain high efficient solar cells,[44] and the small molecular size, high solubility and amorphous nature of spiro-OMeTAD facilitates a good pore filling.

Contact between the FTO anode and TiO_2 could form a Schottky barrier, causing a band bending of the conduction band and inhibiting electron collection. This issue is partially solved by controlling the spray-pyrolysis of the compact TiO_2 layer. This deposition cause a high density of oxygen vacancies, which leaves two extra electrons that dope the TiO_2, causing its Fermi level to be higher than that of the FTO.

Today liquid solar cells reached a structure close to optimal, with excellent stability under long-term illumination and elevated temperatures,[45] but they need to scale up device to large-area arrays to achieve commercial success.

Solid state devices need to enhance electron transport in the mesoporous metal oxide and increase electron lifetime to obtain efficiencies comparable to liquid devices. Power efficiency conversion of over 11%[46] has been achieved, but devices lifetime is too short for commercialization, mainly due to de-wetting and clustering of the hole transporter material.

Solar Cells based on organometal-halide perovskites

Starting from the concept of Dye-Sensitized Solar Cell, in 2009 Miyasaka[47] and co-workers reported the first perovskite-sensitized TiO_2 solar cell. Perovskite are a class of compounds with a crystal structure shown in Figure 1.13a. The devices was built deposing lead bromide perovskite ($CH_3NH_3PbBr_3$) on the TiO_2 film with a spin-coating procedure with the precursor solution containing CH_3NH_3Br and $PbBr_2$, obtaining nanocrystalline particles approximately 2-3 nm in size, and using liquid electrolytes based on iodide and bromide. The device showed an

efficiency of 3.1%.

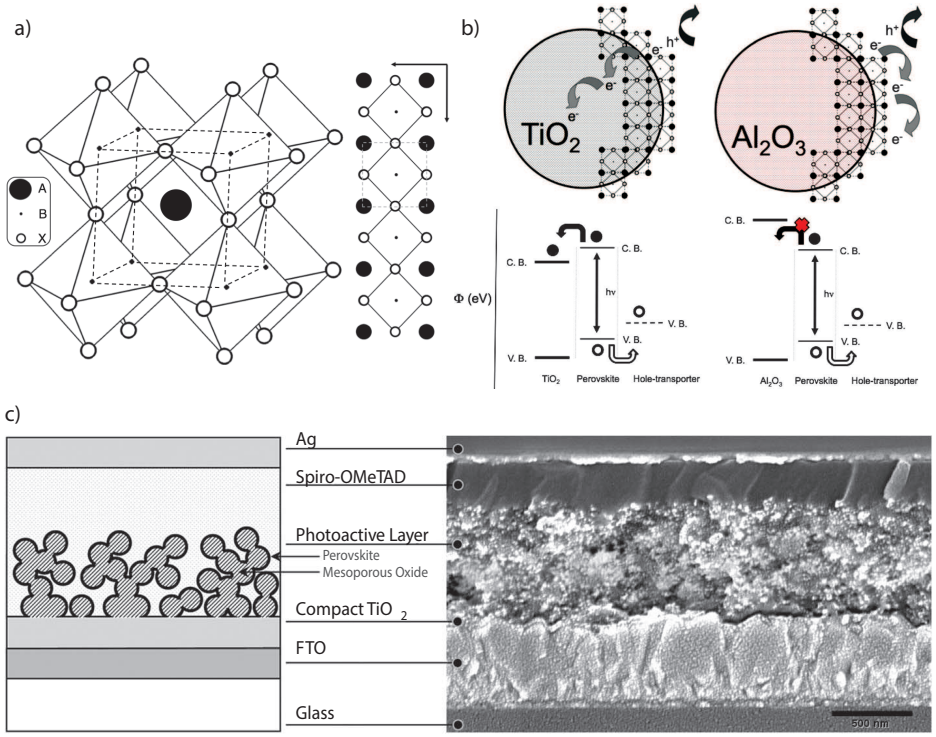

Figure 1.13: Three-dimensional schematic representation of perovskite structure, ABX_3 where A = CH_3NH_3, B = Pb, and X = Cl; b) Cartoon illustrating the charge transfer and transport in a perovskite sensitized TiO2 solar cell, (left) and a non-injecting Al2O3 based perovskite solar cell, (right); c) Schematic representation of full device structure, where the mesoporous oxide is either Al2O3 or anatase TiO2 (left), Cross-sectional SEM image of a full device incorporating mesoporous Al2O3 (right). Adapted from [48]

Later in 2011 Park[49] and co-workers reported on the improved efficiency of TiO_2 solar cells sensitized with lead iodide perovskite ($CH_3NH_3PbBr_3$) using a $Pb(NO_3)_2$ to obtain surface modification of the TiO_2 film before coating the perovskite, such that $Pb(NO_3)_2$ acted as a blocking layer in the solar cells. Device efficiency was 6.5%.

In 2012 Lee et al.[48] realized a solid state device based on perovskite ($CH_3NH_3PbI_2Cl$) absorber coated on the surface of an insulating Al_2O_3 film, that acts purely as a mesoporous scaffold for the perovskite. Electrons cannot inject into the Al_2O_3 and are directly transported to the surface of the FTO electrode. Holes are instead transported to the counter electrode through a layer of spiro-OMeTAD. The perovskite thus acts to perform both light absorption and electron transport. Diffusion in the Al_2O_3 based device was found to be 10 times than in the TiO_2 device, demonstrating the superior photovoltaic performance of the perovskite

solar cell based on an insulating metal-oxide layer. IPCE curve show a maximum value greater than 80% at 400 nm, and the values are maintained greater than 60% up to 700nm. Device efficiency was 10.9%.

The same group reached in 2013 12.3% efficiency using a device based on perovskite $CH_3NH_3PbI(I_{3-x}Cl)_x$ on a mesoporous Al_2O_3 film.

The main issue of perovskite-based solar cells is their high sensitivity to ambient humidity, so anhydrous starting materials need to be used during synthesis.

In 2013 Burschka et al.[50] reported a device with a structure of TiO2/perovskite /spiro-OMeTAD/Au which exhibited a PCE of 15.0%, and when the device was encapsulated under argon, it could maintain more than 80% of its initial PCE after 500 h.

The most performing device, realized by Seok from the Korean Research Institute of Chemical Technology, reached 17.9% as certified from NREL in may 2014[51], but no details about the device have been published yet.

1.3.3 Quantum Dots Solar Cells

If we consider a semiconducting structure in which carrier motion is confined in all directions, typically a nanocrystal of the order of a few nanometers (comparable to the exciton Bohr radius) the system can be described by Schrödinger equation shown in (1.1), where the potential energy $U(\vec{r})$ can be approximated to 0 in the region of the confinement, and to $+\infty$ outside the confinement. Solutions of the equation shows that in this structure the energy gap is enhanced with respect to the bulk value:

$$E = E_g + \frac{\hbar^2 \pi^2}{2\mu R^2} + E_C \tag{1.11}$$

where R is the nanocrystal size, μ is the reduced mass of the electron-hole pair, and E_C is an extra contribution to the energy gap due to Coulomb interaction, $E_C \propto R^{-1}$, which is usually negative for a single-exciton state, but can be positive for multiexciton states.

We can so change energy level spacing controlling particle size without changing other properties of the materials.

As carrier energy spacing is larger than typical phonon quanta, we can expect a reduction in the dissipation efficiency of the phonon bath, so we can have generation of more than one e-h couple on absorption of a single photon. This process is called multiexciton generation (MEG).

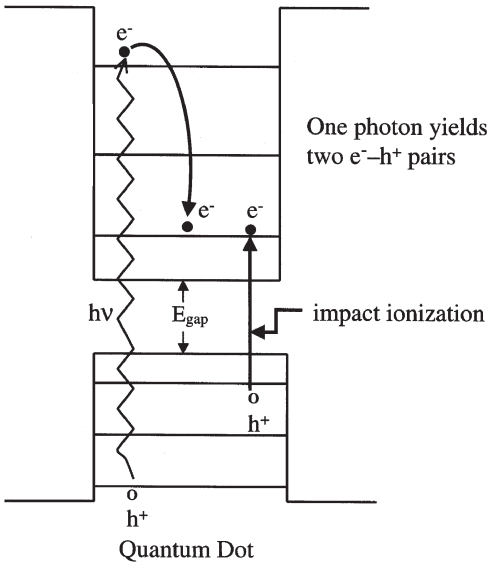

Figure 1.14: Multi Exciton Generation (MEG) via impact ionization process. Adapted from [52]

There are mainly three different mechanisms that can lead to MEG.

- **Impact ionization process**, where a high-energy carrier relaxes to its ground state and excites valence electrons across the band gap producing additional e–h pairs. This process is the reverse of Auger recombination, and the two compete, but at high excitation energy theory predicts that impact ionization is more efficient than Auger recombination and electron–hole relaxation.

- **Coherent mechanism**, where a photon of energy greater than twice the band gap creates a coherent superposition of degenerate single and multiexcitons states due to the strong Coulomb interaction of carriers confined in NCs. The electronic population oscillates between the single exciton state and the multiexciton state. Thermalization of a single exciton is slower than the multiexciton state, so the energy decay faster when the system is in the multiexciton state, favoring its stabilization.

- **Direct mechanism**, where a photon generate a multiexciton state directly, with a process described by second-order perturbation theory.

MEG in photovoltaics could avoid wasting of photon energy exceeding the gap, which usually dissipate their energy into phonons, yealding to an heating of the device and a loss of energy.

This effect is however competitive with the fast inelastic e–h Coulomb interaction mediated scattering. In nanocrystals this process is highly efficient because due to the small size of the structure, e–h Coulomb interaction is stronger and because due to large hole effective mass and valence degeneracy, the hole level spacing is much smaller than the electron one, making a dense manifold, almost a continuum, in which holes can quickly relax emitting phonons.

Inorganic semiconductor quantum dots (QDs) have been extensively investigated as new photosensitizers or light absorbers to replace conventional organic-type sensitizers in DSSCs because of their tunable energy band gaps, large optical absorption coefficients, large dipole moments for enhanced charge separation, and multiple exciton generation.

One of the most intensively studied system is formed by Cadmium-chalcogenide QD-based solar cells. Photoactive materials of these cells are cadmium sulfide (CdS), cadmium selenide (CdSe), cadmium telluride (CdTe) and their alloy nanocrystals. Their optical band gap are represented in Figure 1.15. Solid-state solar

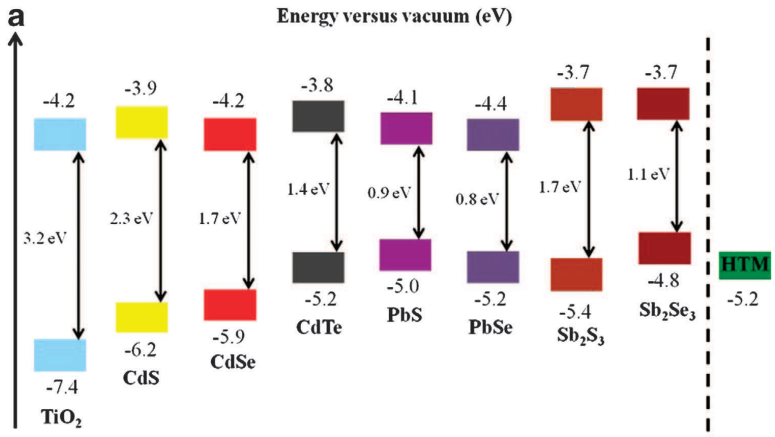

Figure 1.15: Energy levels vs vacuum of various metal-chalcogenide quantum dots (QDs) as prospective light absorbers for hybrid mesoscopic solar cells. The particle sizes are shown in parentheses for TiO2 (bulk), CdS (5nm), CdSe (3 nm), CdTe (3.8nm), PbS (2.4 nm), PbSe (4.5nm), Sb2S3 (5nm), Sb2Se3 (5nm). Adapted from [53]

cells based on CdS, CdSe and CdTe QDs have shown PCEs less than 6% because of their large band gaps, slow electron injection rates and charge recombination at the TiO_2/QD/HTM interfaces. Thin-film solar cells made of $CdSe_xTe_{(1-x)}$ alloys (x=0.9, or 0.8) exhibited an efficiency of $\sim$ 7.1%, smaller than the CdTe-only device (PCE=7.3%), probably due to low efficient electron transport and charge collection through the alloy layers. The ideal cadmium chalcogenide QDSC de-

vices should have a large recombination resistance, a small chemical capacitance and a small series resistance due to a decreased rate of recombination and fewer trap sites at the TiO_2/QD interface. Furthermore, the device performance of the CdTe/CdSe QDSCs can be further improved by increasing the QD loading on the TiO2 film to enhance the efficiency of light harvesting.[53]

Another intensively studied system is formed by lead-chalcogenide QD-based solar cells because of the small band gaps, which allow solar energy harvesting in the near-infrared region. For example PbS QDs have energy gap in the range of 0.9-1.1 eV, and the optical absorption edge can be extended to ∼1300 nm; for PbSe QDs gap energies are tunable from 0.7 to 1.7 eV varying the sizes of QDs. Devices with PbSe QDs treated with hydrazine show an external quantum efficiency (EQE) of 114% and internal quantum efficiency (IQE) of 130%, proving the MEG effect.[54]

Also antimony cahalcogenide QDs have been used in device fabrication. SbS_3 deposed on a mesoporous TiO_2 film have a particle size of $\sim\ 5-10$ nm and an excellent match of energy levels for electron injection and transport. Devices showed IPCE values between 70% and 90% with various hole transporting materials. Highest device performance showed a value of 6.3% using PCPDTBT as HTM layer, but theoretical simulations have shown an optimized efficiency of $\sim 8.5\%$.[55]

1.4 Benchmark parameters

In this section we will see the main parameters to quantify solar cell performances. The key characteristics of a solar cells are the short circuit current density (J_{SC}), open circuit voltage (V_{OC}), fill factor (FF) and PCE, measured with an incident power density of 1000 wm^{-2}, with a light spectrum defined by the Air Mass 1.5[56] standard and at a temperature of 25 °C.

Let us consider a simple electric circuit with a solar cell connected to a load. If exposed to light, it develops a voltage. The voltage developed when the terminals are isolated (or an infinite load) is called *open circuit voltage*. If we connect the terminals with no load, we will see a current density flowing, called *short circuit current density*. For any intermediate load R resistance the cell develops a voltage between 0 and V_{OC} and delivers a current density such that V=IR, and I(V) is determined by the current-voltage characteristic of the cell under that illumination.

1.4.1 Short Circuit current density (J_{SC})

Photocurrent generated by a solar cell under illumination at short circuit is dependent on the incident light. If we define the quantum efficiency (QE) as the probability that an incident photon of energy E will deliver one electron to the external circuit, we can write

$$J_{SC} = q \int b_s QE(E) dE \tag{1.12}$$

where $b_S(E)$ is the incident spectral photon flux density.

1.4.2 Open Circuit Voltage (V_{OC})

Most solar cells can be schematized as diodes. When the device is connected ta a load in dark conditions, a potential difference generates a current which flow in the opposite direction to the photogenerated current. For an ideal diode, the dark current density is given by

$$J_{dark} = J_0(e^{qV/kT} - 1) \tag{1.13}$$

where J_0 is a constant, k is Boltzmann's constant and T is temperature in degrees Kelvin. The overall response of the cell gives the J(V) curve

$$J_{SC} = J_{SC} - J_{dark} \tag{1.14}$$

In the open circuit situation, no current flows into the device, this means that dark current and photogenerate current have the same value. This allow to have an approximate relation (remembering the ideal diode approximation) between V_{OC} and J_{SC}:

$$V_{OC} = \frac{kt}{q} ln(\frac{J_{SC}}{J_0} + 1) \tag{1.15}$$

With some energetic consideration we can also have an estimation of the maximum V_{OC} that a device can reach in ideal conditions.

The general kinetic expression for the current density of electrons $J_n(x)$ through a device is[57]

$$J_n(x) = n(x)\mu_n \nabla U(x) + kT\mu_n \nabla n(x) \tag{1.16}$$

where $n(x)$ is the electrons concentration, μ_n is the electron mobility, k is the

Boltzmann's constant and T is the absolute temperature. An analogous equation can be written for holes.

Let now consider the definition of the quasi Fermi level for electrons in a semiconductor:

$$E_{Fn}(x) = E_{cb}(x) + kT \ln\left(\frac{n(x)}{N_c}\right) \tag{1.17}$$

where $E_{cb}(x) = U(x) + const.$ is the electrical potential energy of the conduction band edge, and N_c is the density of electronic states at the bottom of conduction band. Taking the gradient from 1.17 and substituting it into 1.16 we obtain[57]:

$$J_n = n(x)\mu_n \nabla E_{Fn}(x) \tag{1.18}$$

and analogous for holes.

Since E_{Fn} and E_{Fp} are the driving forces for carrier fluxes, net current must stop when these gradients either simultaneously become zero. The maximum photovoltage in an ideal PV cell is thus given by the maximum splitting between the quasi Fermi levels anywhere in the cell at open circuit, since an applied potential difference grater than this will cause the photocurrent to reverse its direction.

$$V_{OC,max} = \frac{(E_{Fn} - E_{Fp})_{\max}}{q} \tag{1.19}$$

1.4.3 Fill Factor (FF)

The solar cell, in the photovoltaic regime, produce a power density given by

$$P = JV. \tag{1.20}$$

P reaches a maximum at the cell's operating point or *maximum point*, with a corresponding V_m and J_m (that are not the maximum voltage or current density, but the values at which we have maximum power density). The fill factor is defined as the ratio

$$FF = \frac{J_m V_m}{J_{SC} V_{OC}}. \tag{1.21}$$

Referring to the J(V) curve, this value is the ratio between the rectangle drawn by J_{SC} and V_{OC} and the rectangle of V_m and J_m. The value represents then

the "squareness" of the curve, and a value as close as possible to 1 is desirable, because it means that with an optimum load the cell delivers both the maximum photocurrent and photovoltage it can produce.

1.4.4 Power Conversion Efficiency (PCE)

power conversion efficiency is the main parameter to quantify solar cells quality. It is defined as the power density delivered at operating point as a fraction of the incident light power density:

$$PCE = \frac{J_m V_m}{P_S}. \tag{1.22}$$

It can be related to J_{SC} and V_{OC} using FF

$$PCE = \frac{J_{SC} V_{OC} FF}{P_S}. \tag{1.23}$$

CHAPTER 2

Materials and methods

2.1 Introduction

As seen in the previous chapter, a broad range of materials have been employed in solar cells in the past, but often they involved toxic elements or high production costs. In this chapter two promising materials for a cost-effective and environmental friendly photovoltaic application, bismuth(III) sulfide (Bi_2S_3) and copper(I) sulfide (Cu_2S) will be presented and proposed for solar cell application. The former one has been implemented in different device architectures. In the following the device geometries and the experimental procedures to realize them will be illustrated. The latter regards experiments about synthesis procedures. A new technique for a solution process deposition has been tried, and products have been optically characterized.

2.2 Solar cells based on bismuth(III) sulfide

Bismuth sulfide (Bi_2S_3) is a toxic-free and earth-abundant material. It can be found naturally in the form of bismuthinite, which has a lead-grey streaked colour with a metallic luster.[58]

It has an orthorhombic crystal structure with 4 molecules per unit cell. Each molecule contains two bismuth atoms and 3 sulfide atoms which add up to 20 atoms per unit cell (Figure 2.1).

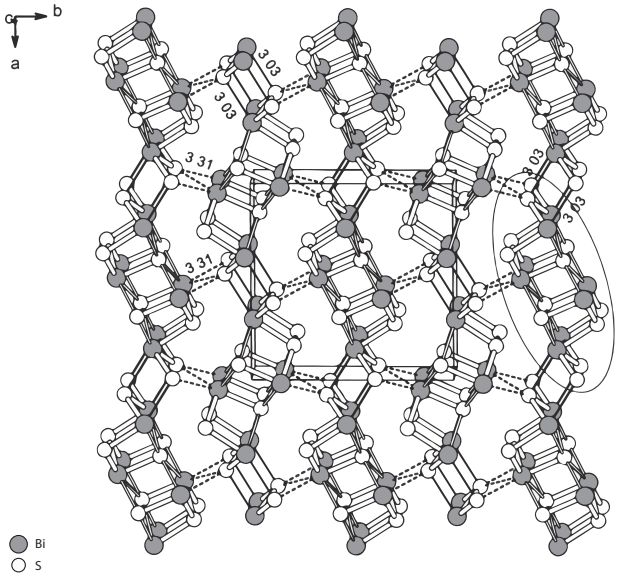

Figure 2.1: Single crystal structure of Bi_2S_3. Adapted from [59]

Bi_2S_3 is a photoconducting semiconductor with a high absorption coefficient (magnitude order 10^5 cm^{-1}) and a ∼1.3 eV direct band gap for bulk material[60] which is very favourable for photovoltaic application. The existence of such material in colloidal nanocrystalline phase makes it suitable for large area solution-processed devices, in fact the number of published papers on this material has grown exponentially in the last two decades.[60,61,62]

The very first study on this material as semiconductor sensitizer goes back to 1994, by Vogel et al.,[63] and in 2008 Kostantatos et al. employed it in high performance photoconductive detectors.[62]

Bismuth sulfide used in this work is supplied by Dr. Daniela Marongiu of Dipartimento di Fisica of Università di Cagliari. The material is made of nanorods of Bi_2S_3 (size ∼20 nm x 15 nm) capped with oleic acid and dispersed in toluene.

In the following sections a study of this material in solar cells will be presented, focusing on the analysis of the performances of devices with different geometries and combined with different materials.

2.2.1 Device structure

We tested material performance in different device architecture, which recall the devices concepts presented in the previous chapter.

a) planar structure FTO/Bi_2S_3/HTM

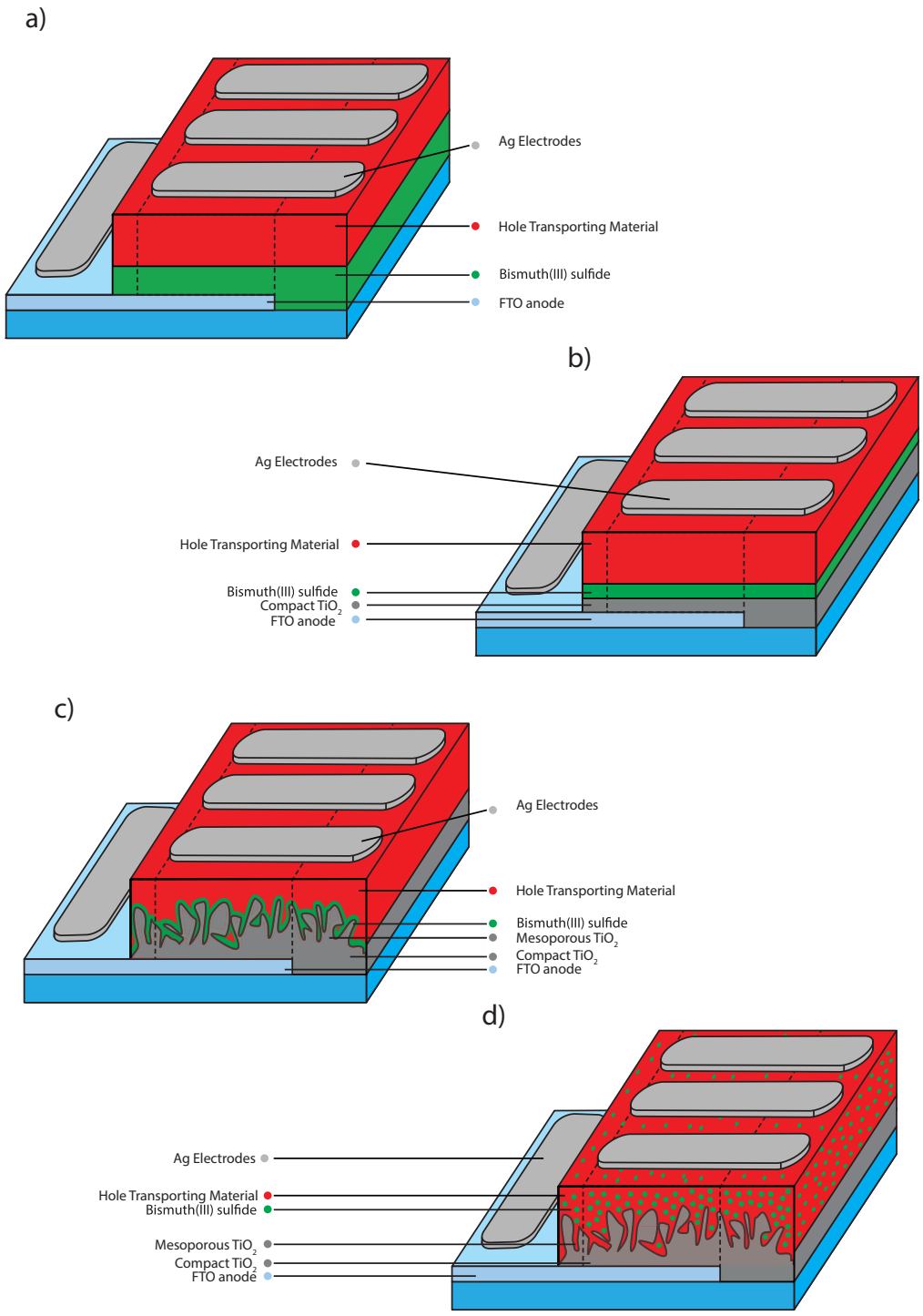

Figure 2.2: Picture of structures tested with Bi_2S_3. Dotted lines represent the active area.

b) planar structure with a hole blocking compact layer FTO/cp-TiO_2/ Bi_2S_3/ /HTM

c) Structure with a mesoporous layer of TiO_2 FTO/cp-TiO_2/mp-TiO_2/ Bi_2S_3/ /HTM

d) Structure with a mesoporous layer of TiO_2 and blend of HTM and Bi_2S_3 nanoparticles FTO/cp-TiO_2/mp-TiO_2/Bi_2S_3:HTM

The first structure is the planar heterojunction, shown in Figure 2.2a. Soda lime glass is used as substrate and FTO is used as transparent anode. A layer of ∼200 nm Bi_2S_3 is deposed as light absorbing and n-type material. A layer of ∼100 nm HTM is then deposed, and silver electrodes are evaporated. The hole transporting materials tested are spiro-OMeTAD and P3HT. The first has shown good performances in DSCs, and the small molecular size, high solubility and amorphous nature (See 1.3.2) should potentially fit very well with the high rugosity of Bi_2S_3 layer, composed by nanorods of about 20 nm x 10 nm. P3HT has been widely reported as good hole transporting material, especially in organic photovoltaic (see 1.3.1), and offer the opportunity to compare our results with some literature works realized in past years.[64]

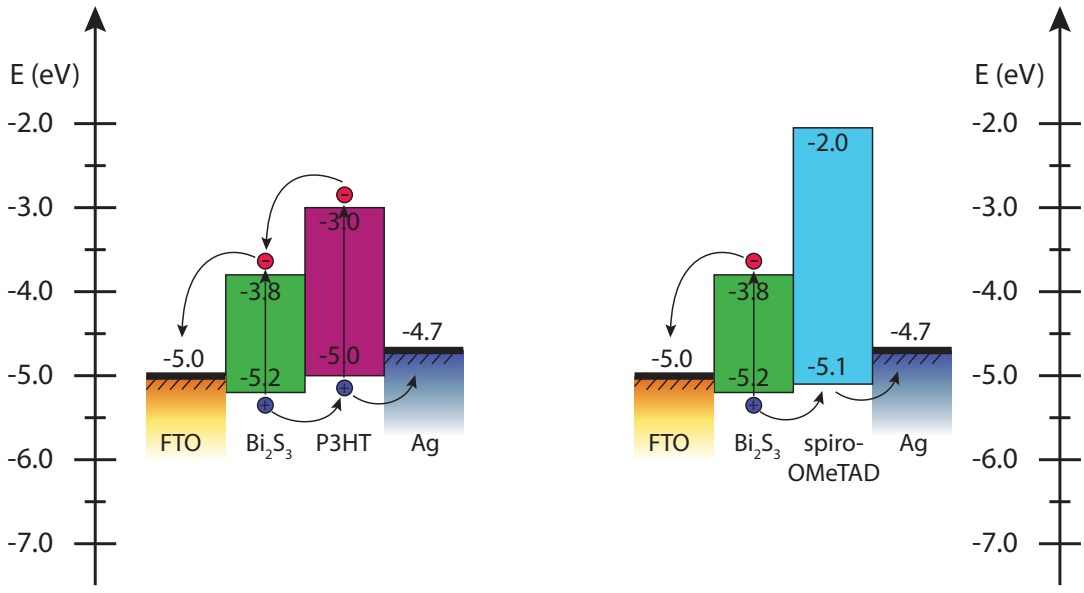

Figure 2.3: Band diagram of the planar heterojunction structure. Values are referred to the vacuum level. Picture on the left represents band configuration in devices with P3HT as hole transporting material; on the right devices with spiro-OMeTAD.

The second structure is shown in Figure 2.2b. The main difference from the previous lays in a ∼100 nm compact TiO_2 layer, which we expect to act as hole blocking layer. The expected energy bands configuration is shown in Figure 2.4.

The third structure we tested has the DSCs structure seen in 1.3.2, with the addition of a mesoporous layer of ∼300 nm TiO_2 (see Figure 2.2c). In this way we increase the surface between bismuth sulfide and TiO_2 layers, in order to achieve a better charge separation. Note that pore size of mesoporous TiO_2 is comparable with Bi_2S_3 NCs size, so we must take into account a non effective pore filling interpreting our results.

In the last structure bismuth sulfide nanocystals are mixed with the hole transporting materials, to test this material in a structure that recalls the blend of fully organic solar cells.

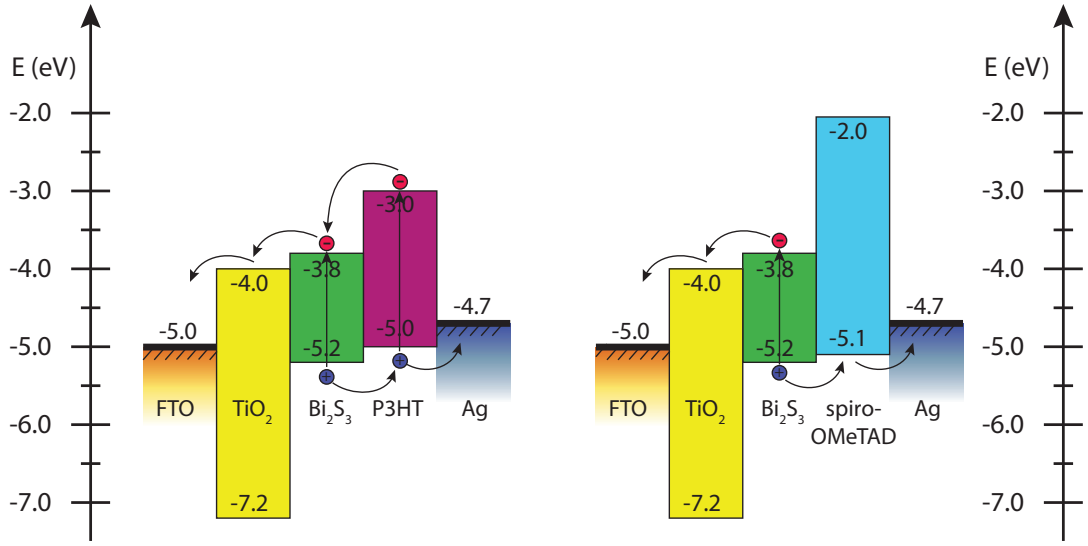

Figure 2.4: Band diagram of the structure with the TiO_2 layer. Values are referred to the vacuum level. Picture on the left represents band configuration in devices with P3HT as hole transporting material; on the right devices with spiro-OMeTAD.

2.2.2 Experimental

In this section we will illustrate the experimental details of fabrication processes of the structures above presented. The process consist briefly in the following steps:

- FTO glass substrate cleaning and electrode patterning;

- Spray pyrolysis of compact TiO_2, only in samples with geometry b), c) and d);
- Mesoporous TiO_2 deposition, only in samples with geometry c);
- $TiCl_4$ treatment, only for samples b) c) and d);
- Bismuth(III) sulfide deposition, for all samples except d);
- Deposition of the Bi_2S_3:P3HT blend only for samples d);
- Spin coating of the hole transporting material for all samples except d);
- Electrode evaporation.

A final paragraph will be dedicate to describe the electrical characterization of solar cells.

FTO glass substrate preparation

Dyesol™ TEC15 Glass Plates are used as substrates for the devices, consisting in 2,3 mm-thick soda-lime glass sheets with a $\sim$ 300 nm FTO conducting coating, (15 Ω/m^2). A slide of 80 mm x 80 mm is cut and from each slide are obtained 20 substrates 14 mm x 14 mm, as shown in Figure 2.5. To avoid short circuits on the final device a stripe of 4,5 mm of the FTO film (the gray stripe of Figure 2.5) is removed via wet etching, using a solution of HCl 0.074 wt. % in water as etching agent and zinc powder as catalyst. Substrates are hence thoroughly cleaned sequentially with bi-distillate water, pure acetone and pure 2-propanol to remove impurities. A final cleaning process of 5' with oxygen plasma is performed, to remove any organic residual.

Spray pyrolysis of compact TiO_2

After the cleaning process a $\sim$100 nm compact layer of TiO_2 is deposed via the spray pyrolysis method.

A precursor solution of anhydrous titanium diisopropoxide bis(acetylacetonate) (75 wt. % in 2-propanol) as titanium source and anhydrous ethanol as solvent is prepared in a volume ratio of 1:10. For a 80 mm x 80 mm substrate, 8,8 ml of solution result in an uniform layer of compact TiO_2 of $\sim$100 nm thickness. Substrate are slowly heated at 400°C on a hotplate in air, afterwards a solution is sprayed uniformly upon the substrate. The solution is atomized by a pneumatic

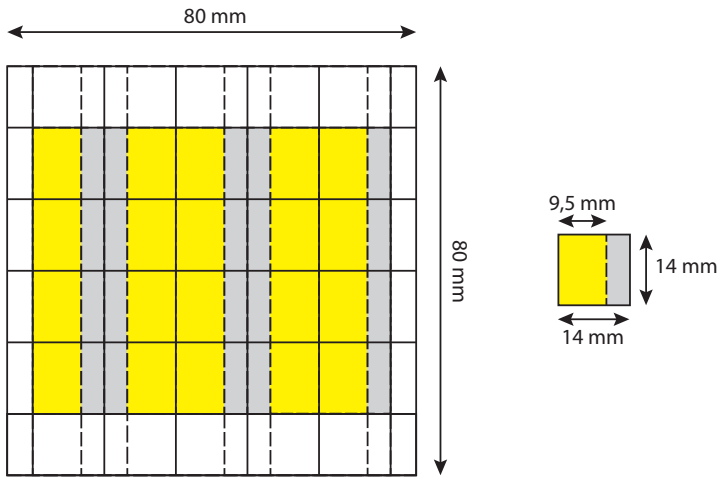

Figure 2.5: Schematic picture of patterned glass slides. The 80 mm x 80 mm slide contains 20 substrates. The yellow part will be the active area of the final device, the gray stripe is removed via wet etching to avoid short circuits after the cathode deposition.

spray system using oxygen as carrier gas. After the spray pyrolysis, substrate is kept at 400° for 20 minutes and then cooled down at atmosphere temperature.

Mesoporous TiO_2 deposition

The mesoporous layer of TiO_2 is deposed with two different techniques according to the thickness desired.

Films thinner then 500nm are deposed via spin-coating. A Dyesol™ 18NR-T Transparent TiO_2 mesoporous paste, with particle size ∼20nm, is solved in ethanol in a volume ratio of 1:3. The obtained solution is sonicated for hours with a tip sonicator first, and with a bath sonicator then, until an homogeneous solution is obtained. Samples are then put in a spin coater and put in spinning. When they reach the desired speed, 90 μL of solution are dropped and the substrate is kept in movement for 60 seconds. To obtain 400 nm thin layer a speed of 4000 rpm is needed, and with a 5000 rpm rotation thickness results 300 nm.

For thicker layers, in view of a large area and highly reproducible deposition, the screen printing technique can be adopted. The same Dyesol™ 18NR-T Transparent TiO_2 mesoporous paste is solved in a mixture of polymers, terpineol ($C_{10}H_{18}O$), in order to obtain a dense solution, with a concentration of 1,1 mg/mL. The solution is then sonicated as described with tip and bath sonicators until it appear homogeneous.

The screen printer is a machine composed by a woven mesh, with pore size

of the order of hundreds of micrometers, and a squeegee (rubber blade). Paste is placed on top of the mesh, and the squeegee is moved along it pushing the paste through the holes in the mesh, reaching the substrate placed under it. The amount of paste deposed is controlled and depends on paste density, holes dimension (# of threads crossing per square inch), squeegee pressure (p), squeegee spring constant (k), squeegee velocity (v) and distance between mesh and substrate (snap-off). Several mesh with several holes dimensions are available, and all other parameters are adjustable by the operator. An example of parameters and resulting layer thickness is reported in Table 2.1.

mesh #	p (points)	k (points)	v (mm/s)	snap-off (mm)	thickness (μm)
250	5	0	100	1.5	1.92 ÷ 2.02
250	5	0	200	1.5	1.89 ÷ 1.94
250	5	0	200	1.0	1.79 ÷ 1.95
300	5	0	200	1.0	1.31 ÷ 1.38
300	5	0	200	1.5	1.32 ÷ 1.44
300	5	0	100	1.5	1.27 ÷ 1.31

Table 2.1: Screen printer parameters for mesoporous TiO_2 layer deposition

Substrate with mesoporous paste deposed both with spin coating or screen printing, are then slowly heated to 550°C with ramps of over 1,5 hours, and baked at this temperature for 30 min in air to obtain TiO_2 sintering.

For the samples used in experiments with bismuth sulphide, a mesoporous thickness of 300 nm has been chosen, then realized by spin coating.

$TiCl_4$ treatment

$TiCl_4$ treatment is performed to improve solar sell performances as explained in 1.3.2. Samples with compact and mesoporous TiO_2 are immersed in a 15 mM aqueous solution of $TiCl_4$ and oven-baked at 70° for one hour. After oven-baking, the substrates are rinsed with bi-distilled water, dried in air and baked again at 550° for 45min to allow all water expulsion and sintering of TiO2 particles deposed from $TiCl_4$ solution.

Bismuth(III) sulfide deposition

Bismuth sulfide deposition is cured by Dr. Daniela Marongiu from Dipartimento di Fisica of Università di Cagliari. Deposition procedure is made via dip coating.

Samples are sequentially dipped in a solution of colloidal nanoparticles of Bi_2S_3 capped with oleic acid in toluene, then in a solution of 1,2-ethandedithiol (EDT) 1 vol.% in acetonitrile and finally in a solution of pure acetonitrile. With the first dipping nanoparticles are deposed on the substrate; the second solution is used to obtain ligand exchange of the long insulating capping molecules by shorter molecules, since small bidentate thiol molecules have been widely reported to improve the carrier mobility of metal chalcogenide NCs.[65] The last solution is used to wash out any residual. The sequence is repeated for 1 h 30 min, in order to obtain a ∼200 nm thickness film. An annealing process of two hours at 200°C is then carried out.

Spin coating of the hole transporting material

Hole transporting material is deposed via spin coating. For spiro-OMeTAD coated samples, a solution of 90 mg/mL of spiro-OMeTAD in chlorobenzene is prepared. The solution is kept overnight to allow the completely dissolution of spiro-OMeTAD in chlorobenzene. For every milligram of spiro-OMeTAD in the prepared solution, 96 μL of 4-tert-Butylpyridine and 205,5 μL of a 170 mg/ml solution of Li-TFSI in acetonitrile are added just before spinning to obtain a p-doping of the material as explained in 1.3.2.

To obtain a good pore filling of mesoporous substrates, the spin coating is performed in 3 step:

1. a drop of 70 μL is put on the non-rotating substrate for 45 seconds
2. substrate starts rotating at 700 rpm with maximum acceleration for 60 seconds
3. speed is changed to 1000 rpm for 15 seconds.

Samples are then kept in air for one night to let the residual solvent evaporate and to start the doping process of Li^+ ions with oxygen.

For P3HT coated samples, a solution of 30 mg/mL of P3HT with molecular weight of 20000 in chlorobenzene is prepared and kept on a hotplate at 70°C for one hour to obtain a complete dissolution of the material. The solution is then spin coated in two steps to obtain a good pore filling of the mesoporous material:

1. 0 rpm for 30 seconds
2. 1000 rpm for 60 seconds

Samples are then annealed at 110°C for 7 minutes to complete solvent evaporation.

Deposition of the Bi_2S_3:P3HT blend

The Bi_2S_3:P3HT blend is deposed via spin coating. The solution of 20 mg/mL of Bi_2S_3 is mixed with a solution of 20 mg/mL of P3HT with molecular weight of 20000 in toluene, prepared as described in the previous section. Toluene is used instead of chlorobenzene to obtain a homogeneous blend of polymer and nanoparticles. The solution is then spin coated with the following recipe:

1. 0 rpm for 30 seconds
2. 1000 rpm for 60 seconds

A bath for 10 minutes in a solution of 1 mg/mL of tetrabutylammonium iodide ($(CH_3CH_2CH_2CH_2)4N(I)$, TBAI) in ethanol to obtain ligand exchange of the oleic acid. In this process TBAI is used instead of EDT to avoid the use of highly toxic EDT.

Then a bath in pure ethanol is followed to wash out any residual.

A final annealing at 110 °C for 7 minutes is then performed.

Electrodes deposition

Electrode deposition is performed via physical vapour deposition (PVD) using a MBROUN MB-ProVap-3 system. Samples are put on a metallic mask patterned with the desired electrode geometry. A mask with samples is put on a holder covered with a shutter in the evaporator chamber, and a silver wire is put as source in a tantalum boat. Before starting the process, the chamber is vacuumed at $3 \cdot 10^{-}6$ bar. Then an electrical current is set in the boat, which heats up due to the Joule effect. Current flow is increased gradually by the operator until the silver starts to evaporate. A thickness monitor allows to control deposition rate and thickness deposed. When evaporation reach a constant rate of 0.2 Å/s the shutter is opened, and the rate is kept at 0.2Å/s to avoid damages to the hole transporting material by high energetic silver particles. When a layer of 10 nm is deposed, current flow is increased until deposition rate reach 1.0÷1.2 Å/s. When the desired thickness is reached, the main shutter is closed, current flow is slowly reduced to zero and chamber is put again at atmosphere pressure.

Solar Cells Testing

Figure 2.6: Typical set-up for the electrical characterization of a solar cell. Reproduced from [66].

Devices are tested using an *Oriel Instruments Sol3A* Class AAA Solar Simulator. It employs a 450 Watt Xenon source with a 4 x 4 square inches illuminated area filtered by an Air Mass 1.5 filter, in order to reproduce a solar spectrum according to the ASTM G 173-03 standard[56]. The standard defines the measurement surface as an tilted (37°) plane with towards the equator, pointing towards the Sun with zenithal angle 48.2°. Irradiance is 1000 W/m^2 for the standard "1 Sun" measurement.

The devices under test (DUTs) are connected to a Keithley 2420 source-meter digitally controlled, with a 0.012% measurement accuracy and a $5\frac{1}{2}$-digit resolution. The measurement starts by opening the shutter of the xenon lamp and biasing the DUT. The bias range varies from -0.5 V to 1.0 V in 50 linear steps; the resulting current is then measured. From one step to the following, a delay of 0,65 s is maintained to avoid transient effects. Resulting current values are divided by the active area of the cell, to obtain current densities values. From the curve J_{SC}, V_{OC}, FF, PCE values are also calculated.

2.3 Copper(I) sulfide

Cu_xS has been a widely studied material, because the variation of the stechiometry $1 \leq x \leq 2$ provide a range of distinct crystalline phases depending on the temperature, producing a significant variation in electrical conductivity and optical band gap.

The discovery in 1954 of the photovoltaic effect in CdS-Cu_2S structure focused lot of interest on this material by the scientific community, that has been studied until the later half of the 1980s.

Studies on this material were gradually abandoned, mainly because of the strong presence of silicon, which was pushed by innovation in the microelectronics industry, and because the CdS/Cu_2S revealed to be unstable due to diffusion of Cu^+ ions in the CdS layer.

The nowadays need of new materials for photovoltaic application allow us to reconsider this material, that exhibit near-ideal and versatile characteristic for solar energy conversion.

Research and development of synthesis and deposition procedures, as well as the study of ideal materials to be combined with copper sulfide in solar devices, are the key points to an efficient use of this prospective material for solar energy conversion.

In this section, we will show the deposition methods that have been explored in order to obtain copper(I) sulfide films.

2.3.1 Material properties

Copper sulfides, Cu_xS, are a family of chemical compounds which are known to exist in five stable phases in the bulk form at room temperature: with x = 1 (covellite), 1.75 (anilite), 1.8 (digenite), 1.95 (djurleite), and 2 (chalcolite).

When the ratio of Cu to S is much below unity, copper generally is found in more or less regular tetrahedral coordination, as in chalcopyrite. When the Cu/S ratio approaches or is greater than unity, the coordination tends to decrease (as to triangular in covellite, CuS) and become irregular and more complex.

Depending on the composition, the electrical conductivity of the material (p type) can vary significantly: 0.07 $\Omega^{-1}cm^{-1}$ to 2400 $\Omega^{-1}cm^{-1}$ as x is varied from 2 to 1.8.[67]

Due to his high propensity to coexist in its many possible phases, electronic

properties are then poor, with high tendency to be degenerate, with a metallic behaviour.

The chalcopyrite phase, copper(I) sulfide (Cu_2S) can be considered ideal absorber material for solar energy conversion being non-toxic, cheap, abundant, semiconductive and with good absorption characteristics due to its band gap of 1.2 eV, which is nearly ideal for solar photovoltaic applications.

2.3.2 Experimental

Cu_2S synthesis procedure reproduce the work of Maier et al. of 2011,[68] where different metal-sulfide nanoparticles where deposed in situ in a polymer matrix of P3EBT from liquid precursors. In our experiment, we omitted the polymer and tried to depose directly the copper(I) sulfide, studying the behaviour on different substrates and with different annealing temperatures. The substrates are chosen in view of application in devices, so a first, simple deposition was tried on FTO coated glass. The second and third experiments were carried on TiO_2, both compact and mesoporous.

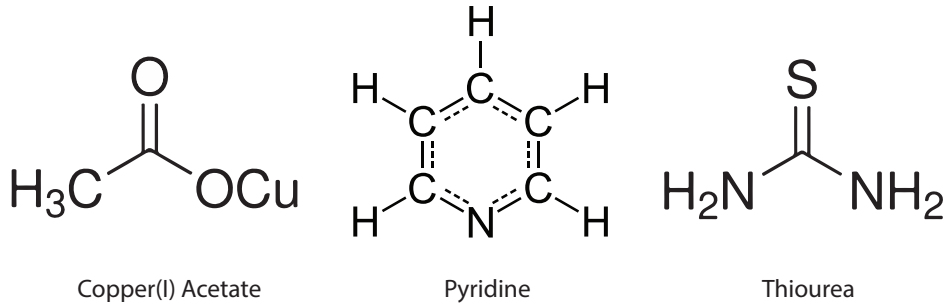

Figure 2.7: Structural formulas of precursors used in copper sulfide deposition

Materials have been deposed via spin coating. In our procedure a metal salt, copper(I) acetate is used as copper source, thiourea as sulphur source and pyridine as solvent (see Figure 2.7)

Substrate preparation

With except of FTO etching, substrates are prepared as explained in 2.2.2. Mesoporous paste is screen-printed to obtain a thickness of 800 nm.

Precursors solution preparation and deposition

A solution of copper(I) acetate 0.30 mol L^{-1} in pyridine is prepared in N_2 atmosphere and stirred on a hotplate at 50°C for 1h. A uniform and opaque solution is obtained. Thiourea is then added in a concentration of 0.75 mol L^{-1}, and the solution is stirred at the same temperature for 2.5 h. A transparent solution is obtained.

Solution is then spin-coated (always in N_2 atmosphere) on substrates dropping 50 μL and spinning for 65 seconds at 1000 rpm, with an acceleration time of 5 seconds.

Samples annealing

To allow solvent evaporation and crystallization of deposed materials, an annealing process in N_2 atmosphere is performed right after the spin coating. To study temperature and time dependence, for every substrate the following temperature and durations have been tried:

- 30 min annealing at 180°C;
- 1 h annealing at 180°;
- 30 min annealing at 200°C;
- 1 h annealing at 200°;
- 30 min annealing at 250°C;
- 1 h annealing at 250°;

During the annealing process, a colour change from transparent to a brownish dark is observed.

Optical characterization

To measure the optical properties of the samples regarding light absorption, a Perkin Elmer Lambda 1050 UV/Vis/NIR spectrophotometer with a 150 mm integrating sphere is used.

The measurements are made with a wavelength range between 350 nm and 1100 nm, and two different measurement of transmittance and reflectance are performed.

Light from an internal source is filtered by a monochromator and is hence shined upon the sample. A sweep of all the wavelength in the range of interest is performed.

To allow the collection also of the light diffused from the sample, measurement are performed with an integrating sphere. This is an optical component consisting in a spherical cavity with its interior coated with a white reflective material. As shown in Figure 2.8, light diffused from the sample is reflected from the internal surface of the sphere and can be all collected from the detector, bot in reflectance and transmittance configurations.

The absorbed light is then given by

$$I_A = I - I_R - I_T \tag{2.1}$$

where I_A is the intensity absorbed, I is the intensity of the source, I_R is the intensity of the reflected light and I_T is the intensity of the transmitted light.

The absorbance is then defined as

$$A(\lambda) = -\log_{10}\left(\frac{I_A}{I}\right) \tag{2.2}$$

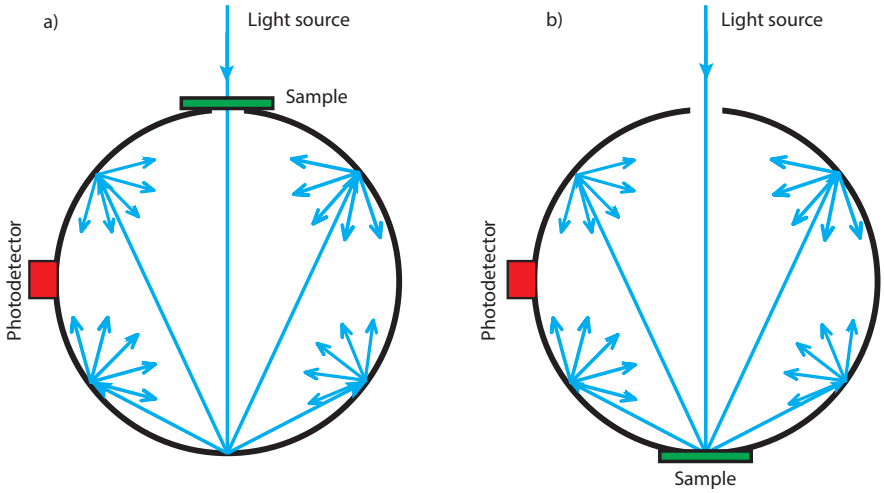

Figure 2.8: Schematic picture of the integrating sphere used in the spectrophotometer. Configuration a) is used in transmittance measurement, while configuration b) is used in reflectance measurement

CHAPTER 3

Results

3.1 Solar cells with bismuth(III) sulfide

In this section we will report and discuss electrical measurement under simulated solar light of devices realized with bismuth sulfide.

3.1.1 Run 1: Test of architectures

3 devices for each structure illustrated in 2.2.1 have been realized, and every device is composed of 3 cells (see Figure 2.2). For every cell JV characteristic has been measured, and from this V_{OC}, J_{SC}, FF and PCE values are calculated.

Performances are summarized in Table 3.1, were benchmark parameter of every device is reported.

From 27 cells fabricated, 8 did not produce any photocurrent, 5 with the FTO/Bi_2S_3/cp-TiO_2/mp-TiO_2/spiro-OMeTAD/Ag structure and 2 with the simple FTO/Bi_2S_3/spiro-OMeTAD/Ag structure. Since there was at least one working device for each of these structures, we can attribute this to uncontrolled factors during the device fabrication, which needs an optimized procedure.

Best performance came from devices using P3HT as hole transporting material, and we attribute this to the contribution of P3HT in absorption and generation of carriers.

Efficiencies are very low, best performances are in the mesoporous structure

with P3HT due to high photovoltage and high photocurrent produced.

structure	V_{OC} (V)	J_{SC} (mA cm^{-2})	FF (%)	PCE (%)
FTO/cp-TiO_2/ /Bi2S3/ /P3HT/Ag	0,18	0,56	47,50	0,043
FTO/cp-TiO_2/ /Bi_2S_3/ /spiro-OMeTAD/Ag	0,25	0,18	39,87	0,018
FTO/cp-TiO_2/mp-TiO_2/ /Bi2S3/ /P3HT/Ag	0,18	0,71	44,27	0,057
FTO/cp-TiO_2/mp-TiO_2/ /Bi2S3/ /spiro-OMeTAD/Ag	0,05	0,08	39,63	0,018
FTO/ /Bi2S3/P3HT/ /Ag	0,12	0,38	36,44	0,017
FTO/ /Bi2S3/spiro-OMeTAD/ /Ag	0,15	0,22	29,45	0,010

Table 3.1: Summary of cell performace

The values are compared in the graphs of Figure 3.1:

- $\mathbf{V_{OC}}$ values of devices with compact TiO_2 layer without mesoporous layer are the best performing, comparable with devices found in literature.[64] This could be due to the presence of an hole blocking layer, that reduces hole injection, hence carrier recombination.

  Devices with a mesoporous layer show inferior V_{OC} values. We can assume this happens because of a non effective pore filling of the Bi_2S_3 nanocrystals (size $\sim$ 10 nm x 20 nm, comparable with pores size).

- $\mathbf{J_{SC}}$ values confirmed the of P3HT as HTM and light absorbing material, as indicated from comparison of devices with same structures but different HTM. Devices show opposite trends, increasing values when P3HT is used with more layers, and decreasing when spiro-OMeTAD is used. One

possible explanation is considering mesoporous structure increase interfaces where excitons generated in P3HT can dissociate, but with a non absorbing material like spiro-OMeTAD, a larger surface has no benefits and implies an increased number of defects, with consequent recombination an losses in current.

- **FF** values are very dispersed, since they strongly depend on interface recombination processes, shunt and series resistance and current produced. Hence the combination of the above factors causes a non correlating distribution, like the one showed in Figure 3.1.

- **PCE** values are then a result of the factors explained, with devices with P3HT showing best values, in particular in the mesoporous structure. However, considering that we focus on bismuth sulfide as light absorbing material, we can state that the most promising structure is composed by the FTO/cp-TiO_2/Bi_2S_3/spiro-OMeTAD/Ag; better performance in the mesoporous structure is achieved thanks to a better current generation in P3HT and not thanks to a better compatibility between this HTM and Bi_2S_3.

J-V curves are reported in Figure 3.2. Curves slope in devices of all structures with spiro-OMeTAD suggest a very low shunt resistance, so we can suppose the device has major defects on the interface between layers.

The high slope of the curve can be interpreted as an alternate current path for light-generated carriers, where power is lost. This can be attributed of a non uniform dispersion of nanoparticles and a possible leakage current. This phenomenon is evident in devices without the TiO_2 layers, which can act as buffer layer, where the slope is steeper. A further study concerning the optimization of the bismuth sulfide synthesis and deposition procedure is strongly desirable.

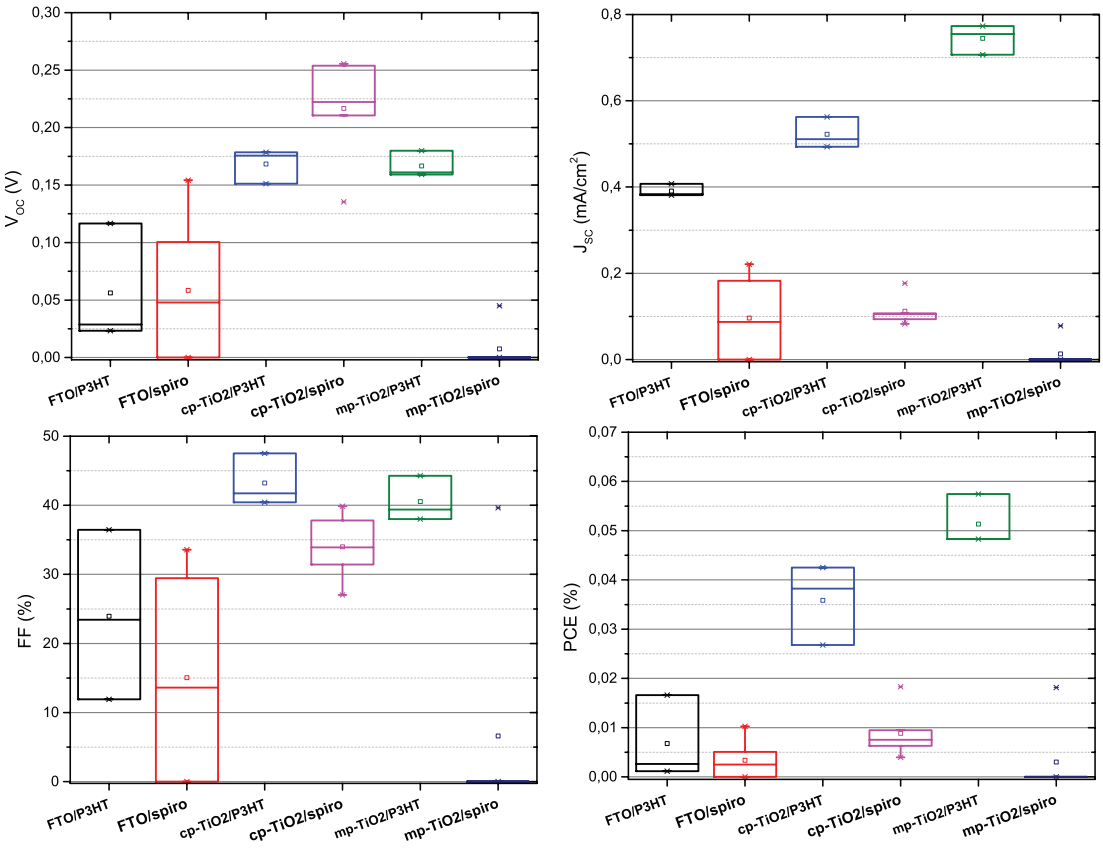

Figure 3.1: V_{oc}, J_{ss}, FF and PCE values obtained in first experiment with solar cells with bismuth sulfide. Labels, from left to right, are referred to the following structure: FTO/Bi_2S_3/P3HT, FTO/Bi_2S_3/spiro-OMeTAD, FTO/cp-TiO_2/Bi_2S_3/P3HT, FTO/cp-TiO_2/Bi_2S_3/spiro-OMeTAD, FTO/cp-TiO_2/mp-TiO_2/Bi_2S_3/P3HT, FTO/cp-TiO_2/mp-TiO_2/Bi_2S_3/spiro-OMeTAD.

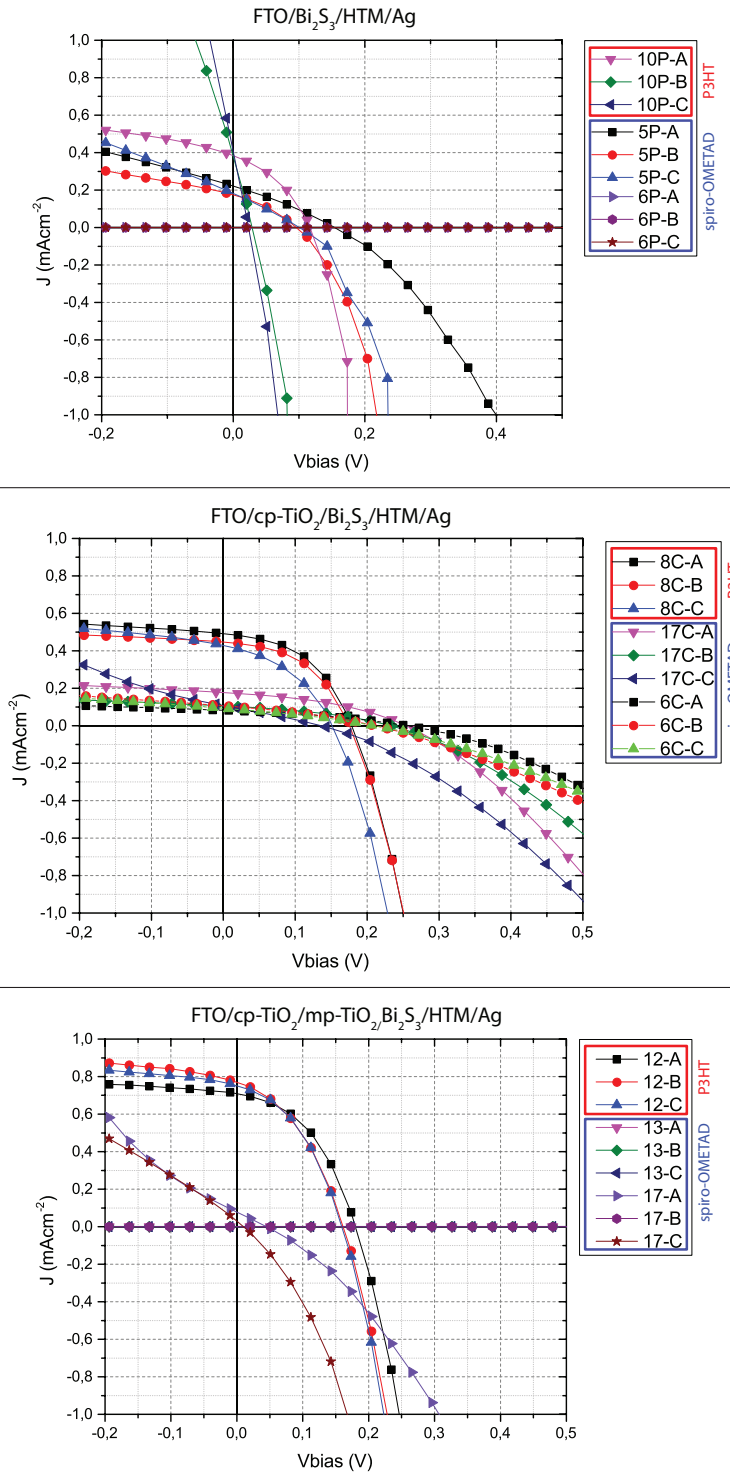

Figure 3.2: JV curves of devices realized with bismuth sulfide. On the top devices with the FTO/Bi_2S_3/HTM structure, in the middle device with FTO/cp-TiO_2/Bi_2S_3/HTM and on the bottom devices with the FTO/cp-TiO_2/mp-TiO_2/Bi_2S_3/HTM structure. Different hole transporting materials used are indicated in the legend.

3.1.2 Experiment 2: Optimized solution

Experiment 2 repeats the previous one, but a new dispersion of Bismuth Sulfide has been used. The new solution provided has been synthetized with an optimized procedure (cured by Università di Cagliari, not reported here) which should assure a better quality of crystals and reduce defects that may cause recombinations, thus low currents.

Figure 3.3 compares the performances of this new run of devices.

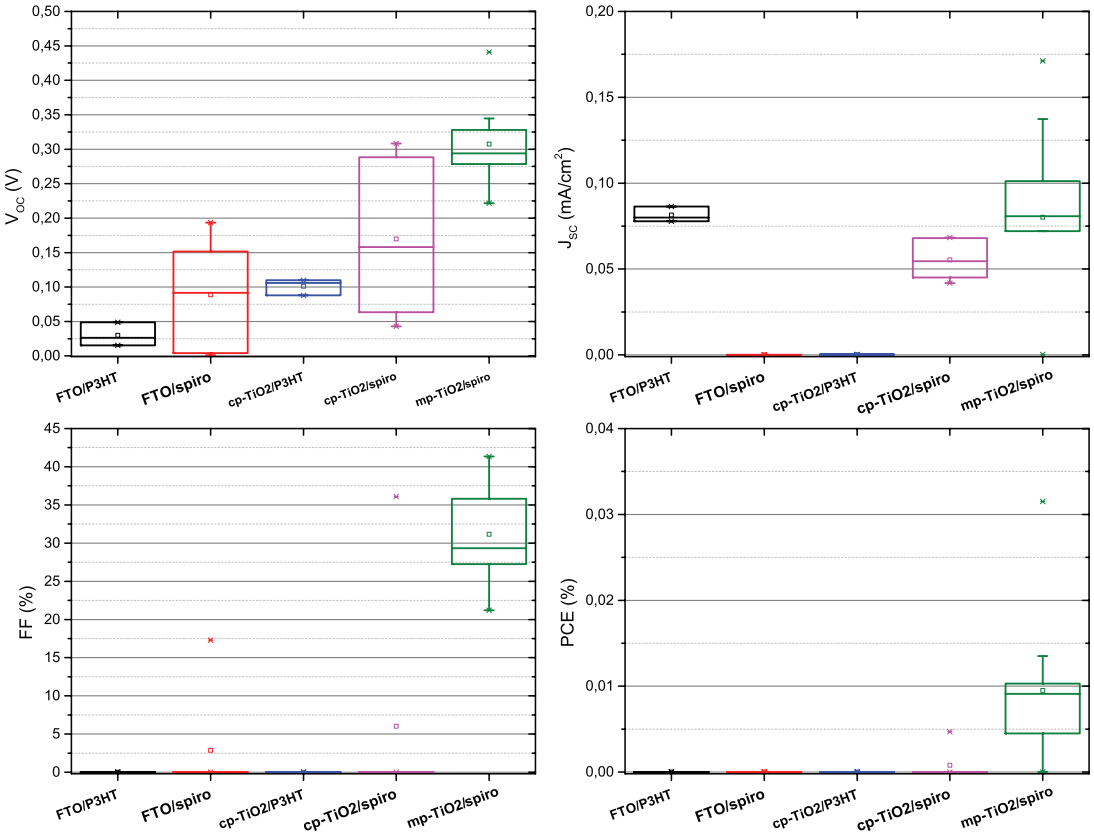

Figure 3.3: V_{oc}, J_{ss}, FF and PCE values obtained in second experiment with solar cells with bismuth sulfide. Labels, from left to right, are referred to the following structure: FTO/Bi_2S_3/P3HT, FTO/Bi_2S_3/spiro-OMeTAD, FTO/cp-TiO_2/Bi_2S_3/P3HT, FTO/cp-TiO_2/Bi_2S_3/spiro-OMeTAD, FTO/cp-TiO_2/mp-TiO_2/Bi_2S_3/spiro-OMeTAD.

As shown in Figure 3.3, most of the cells were not working. The only working devices were among the two last structures, the one with the compact TiO_2 and spiro-OMeTAD as HTM and the one with the mesoporous scaffold. The working devices showed a better Voc compared with the previous experiment, so the problem of defects in the active material appear to be partially solved, but

the photocurrents remain at very low values, then the PCEs could not reach good values.

To investigate the reasons that leads to low photocurrents (hence PCEs), we report here (Figure 3.4 and Figure 3.5) two SEM images of the best performing device.

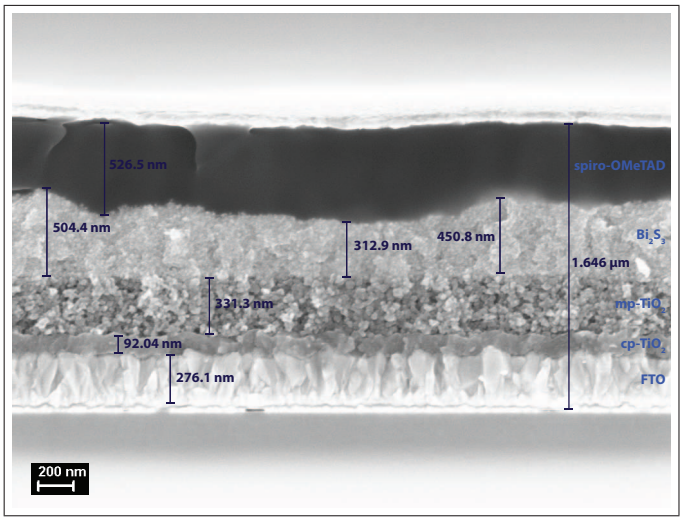

Figure 3.4: SEM image of the solar cell. The structure is as follow: FTO/cp-TiO_2/mp-TiO_2/Bi_2S_3/spiro-OMeTAD.

As shown in Figure 3.4, the layer of Bi_2S_3 appears very irregular. Moreover its thickens, which we expected to be of about 200 nm, varies from 300 nm to 500 nm. This could be caused by the infiltration of the solution of spiro-OMeTAD in chlorobenzene, that could destroy the packaging of nanocrystals resulting in this irregular morphology. The architecture of the device is then highly compromised, and this could be a possible explanation of the low performances and high failure rate.

From the SEM images (see Figure 3.5) is also clear that Bi_2S_3 does not infiltrate into the mesoporous layer of TiO_2, so a reduction of thickness is desirable in future experiments.

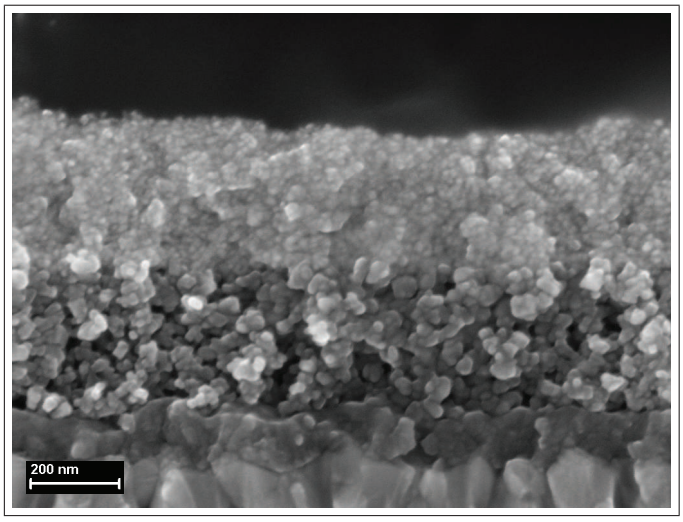

Figure 3.5: SEM image, detail of the Bi_2S_3/mp-TiO_2 interface

3.1.3 Run 3: Bulk etherojunction

The last experiment with bismuth sulfide was performed with the fourth architecture showed in 2.2.1. As in the previous experiment was showed that Bi_2S_3 does not infiltrate into the mesoporous scaffold, in some devices the thickness of mp-TiO_2 was reduced to 100nm. The main issue of this structure is to perform the ligand exchange into the bulk. To investigate this process, in some devices the bath in TBAI dissolved in ethanol was not performed (see Section 2.2.2). In the following Figure 3.6 we report the performance of the devices realized.

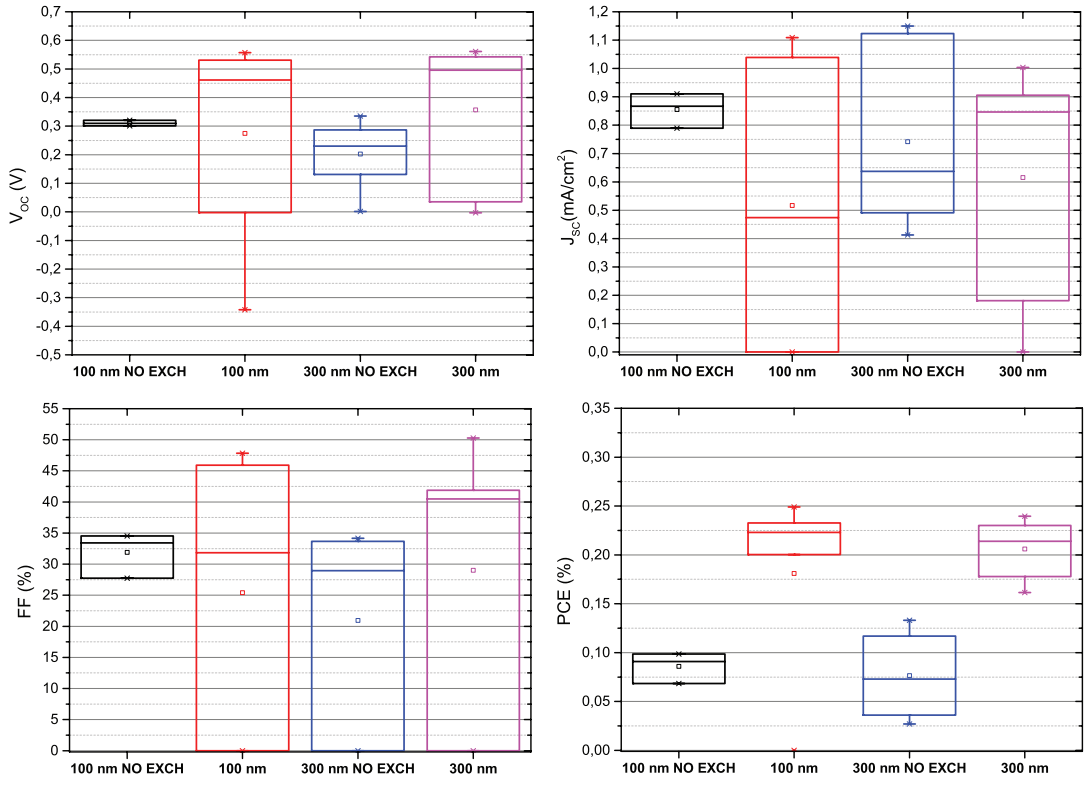

Figure 3.6: V_{oc}, J_{ss}, FF and PCE values obtained in third experiment with solar cells with bismuth sulfide. All samples have the following structure. Labels, from left to right, are referred to the following structure: FTO/cp-TiO_2/mp-TiO_2/Bi_2S_3:P3HT. The thickness of the mp-TiO_2 is 100 nm for the first two columns, 300 nm for the others. Labels "NO EXCH" indicate samples in which no ligand exchange has been performed.

- **V_{OC}** values where a ligand exchange has been performed are the best performing, values are almost doubled compared to values found in literature.[64]

- **J_{SC}** values were still low, even if a small increase is appreciable compared

to previous experiments. No trends related to the ligand exchange process is evident.

- **FF** values are very dispersed, but record values are reached in samples where the ligand exchange has been performed.

- **PCE** clearly show the effectiveness of the ligand exchange process. Efficiency of this kind of devices is one order of magnitude greater than the previous experiments, and record values can be found in devices with a 100 nm thick mesoporous layer.

3.2 Copper sulfide deposition

In this section we will illustrate and discuss the optical absorption measurement of samples involved in copper sulfide deposition.

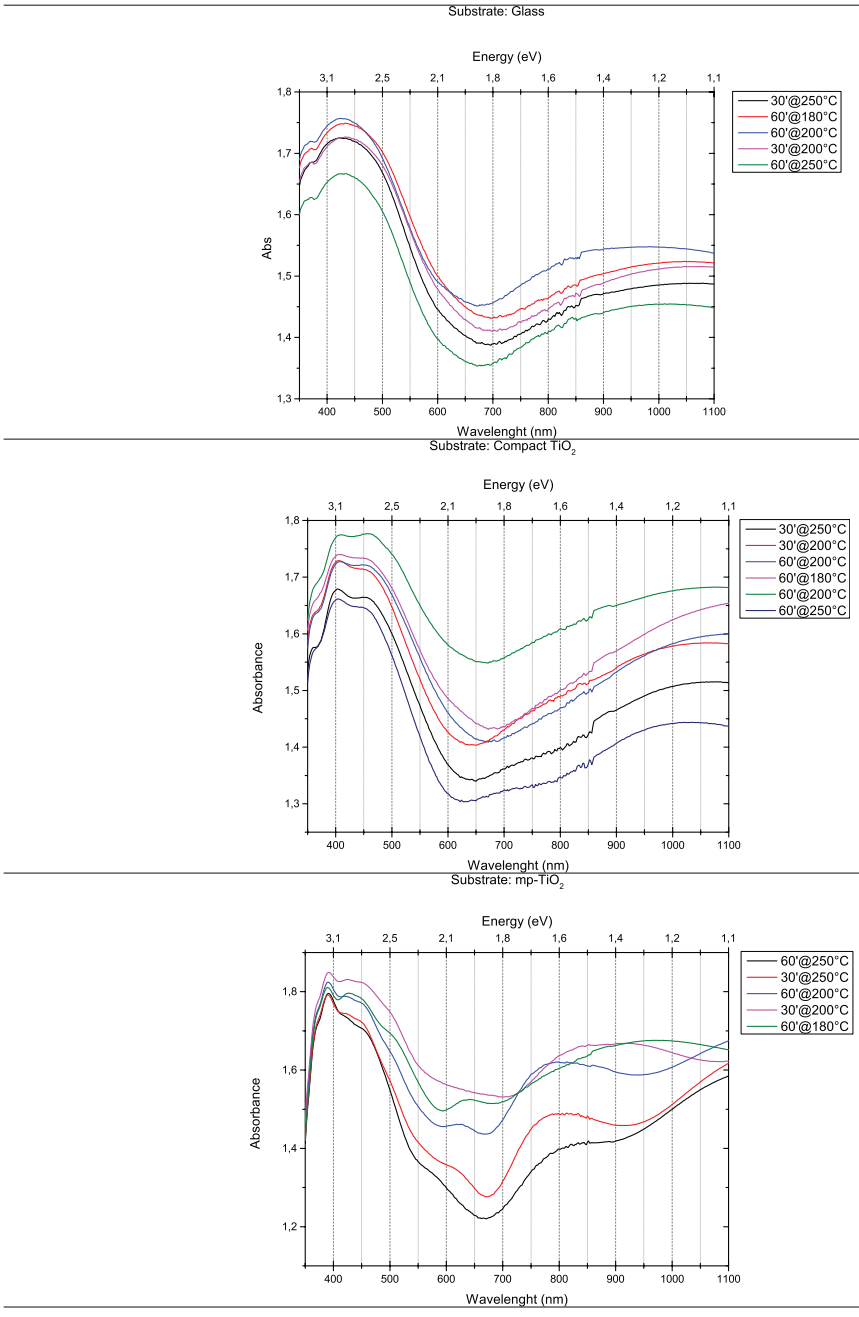

Figure 3.7: Absorbance spectra of deposed Cu_xS. On the top Cu_xS deposed on FTO coated glass; in the middle on compact TiO_2 and on the bottom on mesoporous TiO_2.

Figure 3.7 shows the absporbance of samples with Cu_2S deposed on FTO-

coated glass (bottom graph), compact TiO_2 (middle graph)and mesoporous TiO_2 (bottom graph).

In the first graph of Figure 3.7 the absorption spectra in copper sulfide deposed on FTO-coated glass is shown, with different annealing times and temperatures. Curves follow the same trend and peaks at the same values. From this measurements we can deduce that a 180°C annealing temperature is enough for our synthesis process.

The broad peak around 1050 nm is ascribable to an in-plane localized surface plasmon resonance mode, which dominates the plasmonic response as described by Xie et al.[1] This means that our synthesis did not produce stoichiometric Cu_2S: in that case the peak would be suppressed by the semiconducting behavior of the material.

The same effect is observable on compact TiO_2, where we can also observe a change in shape of the peak at 450 nm. The different shape is probably caused by the presence of a waste product of the chemical reaction trapped in the titanium.

This effect is amplified in the last graph, where the mesoporous structure increased the trapping effect and inhibited the solvent and waste evaporation.

We can see a comparison of curves from samples that received same annealing procedure (30 min at 200 °C) in Figure 3.8. We can observe that the plasmonic peak is stronger on mesoporous structure, and appears to be partially suppressed on compact and glass substrate. This behaviour could indicate that a mesoporous scaffold facilitates the presence of a phase poor in copper.

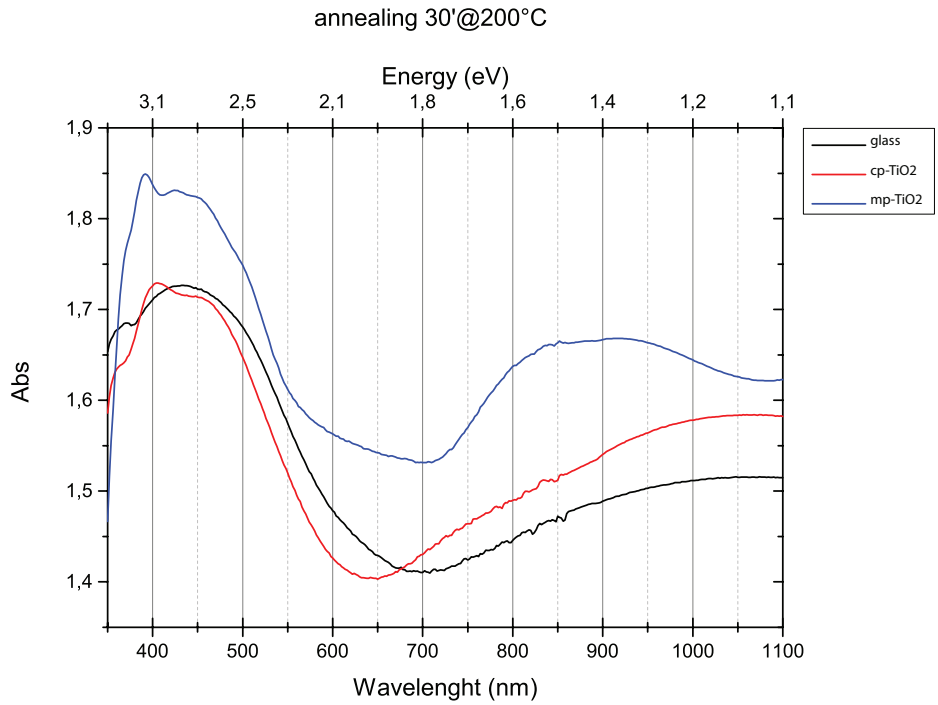

Figure 3.8: Comparison of Cu_2S spectra deposed on different substrates with same annealing treatment. G13 represents Cu_2S deposed on FTO-coated glass, C8 is Cu_2S deposed on compact TiO_2 and M16 is Cu_2S deposed on mesoporous TiO_2.

CHAPTER 4

Conclusions and outlooks

In this thesis work we presented the results of a preliminary, but yet detailed analysis, of bismuth(III) sulfide and copper(I) sulfide, two promising materials for a low cost and environmental friendly photovoltaic applications.

The first material (bismuth(III) sulfide) has been tested in different solar cells in order to evaluate the performances of the material itself. The main goal was to identify the main issues in the production process in order to be able to define the direction of a more detailed R&D activity in the near future; even though the measured efficiency of these devices was quiet poor we reached our goal.

Comparing the material in four different configuration was very useful since it highlighted the effects of a possible non uniform distribution of the nanoparticles at the interface. This dis-uniformity is probably caused by two different factors: a non optimized deposition procedure and a displacement problem caused by the geometry of nanpoarticles. A more detailed and deep analysis provided by scanning electron microscopy showed that the interface morphology is highly compromised by the fabrication procedure.

One solution has been shown to lay in the use of the same nanoparticles, but in a bulk heterojunction structure. A properly designed blend in a polymer bypassed these non uniformity issues, improving the efficiency of one order of magnitude and delivering V_{OC} values higher than those recorded in similar devices presented in literature.

Different electron-transport layer, such as ZnO, or hole extracting layers, like

MoO_3, can be tested to improve the performances of the cells.

Hole transporting materials showed good performance only when used in light absorbing configuration. We can assert that devices with P3HT showed better performances than spiro-OMeTAD because of the photo activity of P3HT itself, and not because of a better intrinsic compatibility with bismuth sulfide. For a stronger confirmation of our explanation, EQE measurement are necessary. A future optimization of the device should probe different p-type materials and characterize charge career generation and separation in the materials.

Another possible study could be done using organometal-halide perovskite, deeply described in 1.3.2 as absorbing material, since it is reported to have encouraging performances also as p-type material.

From the different copper sulfide depositions we performed, we can conclude that our actual technique does not allow to obtain pure copper(I) sulphide; it lead to a mixed phase instead. On this matter, an optimization on reagent concentration has to be put to test. A XRD analysis could easily show the different phases in our sample. A thermogravimetric analysis can be carried on to understand if, especially in the mesoporous substrate, reaction residuals can easily evaporate or need a stronger treatment.

In conclusion, this work intended to be a first and preliminary approach to the use of two promising green materials for photovoltaic application. Tests performed on copper sulfide showed that the procedure partially lead to the desired product, so a study to improve the synthesis has been outlined, while in experiments with bismuth sulfide working devices have been realized and a plan to optimize performance has been designed.

Bibliography

1. Y. Xie, L. Carbone, C. Nobile, V. Grillo, S. D'Agostino, F. Della Sala, C. Giannini, D. Altamura, C. Oelsner, C. Kryschi, and P. D. Cozzoli, "Metallic-like stoichiometric copper sulfide nanocrystals: Phase- and shape-selective synthesis, near-infrared surface plasmon resonance properties, and their modeling," *ACS Nano*, vol. 7, no. 8, pp. 7352–7369, 2013.

2. International Energy Agency, "Key world energy statistics," Paris, 2013.

3. N. S. Lewis, "Toward cost-effective solar energy use," *Science*, vol. 315, no. 5813, pp. 798–801, 2007.

4. S. Wagner, J. L. Shay, P. Migliorato, and H. M. Kasper, "$CuInSe_2$/CdS heterojunction photovoltaic detectors," *Applied Physics Letters*, vol. 25, no. 8, pp. 434–435, 1974.

5. J. L. Shay, S. Wagner, and H. M. Kasper, "Efficient $CuInSe_2$/CdS solar cells," *Applied Physics Letters*, vol. 27, no. 2, pp. 89–90, 1975.

6. M. Alonso, M. Garriga, C. Durante Rincón, E. Hern ández, and M. León, "Optical functions of chalcopyrite $CuGa_xIn_{(1-x)}Se_2$ alloys," *Applied Physics A*, vol. 74, no. 5, pp. 659–664, 2002.

7. B. J. Stanbery, "Copper Indium Selenides and Related Materials for Photovoltaic Devices," *Critical Reviews in Solid State and Materials Sciences*, vol. 27, no. 2, pp. 73–117, 2002.

8. D. J. Schroeder and A. A. Rockett, "Electronic effects of sodium in epitaxial $CuIn_{1-x}Ga_xSe_2$," *Journal of Applied Physics*, vol. 82, no. 10, pp. 4982–4985, 1997.

9. S. Zhang, S.-h. Wei, A. Zunger, and H. Katayama-Yoshida, "Defect physics of the CuInSe2 chalcopyrite semiconductor," *Physical Review B*, vol. 57, pp. 9642–9656, Apr. 1998.

10. T. Nakada, K. Furumi, and A. Kunioka, "High-efficiency cadmium-free Cu(In,Ga)Se_2 thin-film solar cells with chemically deposited ZnS buffer layers," *Electron Devices, IEEE Transactions on*, vol. 46, no. 10, pp. 2093–2097, 1999.

11. Y. Ohtake, T. Okamoto, A. Yamada, M. Konagai, and K. Saito, "Improved performance of Cu(InGa)Se_2 thin-film solar cells using evaporated Cd-free buffer layers," *Solar Energy Materials and Solar Cells*, vol. 49, no. 1-4, pp. 269–275, 1997.

12. D. Hariskos, S. Spiering, and M. Powalla, "Buffer layers in Cu(In,Ga)Se_2 solar cells and modules," *Thin Solid Films*, vol. 480-481, pp. 99–109, 2005.

13. U. Rau and M. Schmidt, "Electronic properties of ZnO/CdS/Cu(In,Ga)Se_2 solar cells - aspects of heterojunction formation," *Thin Solid Films*, vol. 387, no. 1-2, pp. 141–146, 2001.

14. A. Luque and S. Hegedus, *Handbook of Photovoltaic Science and Engineering*. Chichester: Wiley, 2002.

15. G. Lanzani, *The Photophysics behind Photovoltaics and Photonics*. Weinheim, Germany: Wiley-VCH, 2012.

16. W. Demtröder, *Atoms, Molecules and Photons. An Introduction to Atomic-, Molecular- and Quantum Physics*. Berlin Heidelberg: Springer, 2 ed., 2010.

17. H. Frölich, "On the theory of superconductivity: The one-dimensional case," *Proc. R. Soc. Lond. A*, vol. 223, pp. 296–905, May 1954.

18. R. E. Peierls, *Quantum Theory of Solids*. Clarendon, Oxford: Oxford University Press, 1955.

19. S. Karg, W. Riess, V. Dyakonov, and M. Schwoerer, "Electrical and optical characterization of poly(phenylene-vinylene) light emitting diodes," *Synthetic Metals*, vol. 54, no. 1-3, pp. 427–433, 1993.

20. N. S. Sariciftci, L. Smilowitz, A. J. Heeger, and F. Wudl, "Photoinduced Electron Transfer from a Conducting Polymer to Buckminsterfullerene," *Science*, vol. 258, no. 5087, pp. 1474–1476, 1992.

21. G. Yu, J. Gao, J. C. Hummelen, F. Wudl, and A. J. Heeger, "Polymer photovoltaic cells: Enhanced efficiencies via a network of internal donor-acceptor heterojunctions," *Science*, vol. 270, no. 5243, pp. 1789–1791, 1995.

22. P. K. Watkins, A. B. Walker, and G. L. B. Verschoor, "Dynamical monte carlo modelling of organic solar cells: The dependence of internal quantum efficiency on morphology," *Nano Letters*, vol. 5, no. 9, pp. 1814–1818, 2005.

23. F. Padinger, R. Rittberger, and N. Sariciftci, "Effects of postproduction treatment on plastic solar cells," *Advanced Functional Materials*, vol. 13, no. 1, pp. 85–88, 2003.

24. J. Peet, J. Y. Kim, N. E. Coates, W. L. Ma, D. Moses, A. J. Heeger, and G. C. Bazan, "Efficiency enhancement in low-bandgap polymer solar cells by processing with alkane dithiols.," *Nature materials*, vol. 6, pp. 497–500, July 2007.

25. M. Scharber and N. Sariciftci, "Efficiency of bulk-heterojunction organic solar cells," *Progress in Polymer Science*, vol. 38, pp. 1929–1940, Dec. 2013.

26. H. Tributsch and M. Calvin, "Electrochemistry of excited molecules: Photoelectrochemical reactions of chlorophylls," *Photochemistry and Photobiology*, vol. 14, no. 2, pp. 95–112, 1971.

27. H. Gerischer, "Electrochemical techniques for the study of photosensitization," *Photochemistry and Photobiology*, vol. 16, no. 4, pp. 243–260, 1972.

28. R. Memming, "Photochemical and electrochemical processes of excited dyes at semiconductor and metal electrodes," *Photochemistry and Photobiology*, vol. 16, no. 4, pp. 325–333, 1972.

29. H. Tsubomura, M. Matsumura, Y. Nomura, and T. Amamiya, "Dye sensitised zinc oxide: aqueous electrolyte: platinum photocell," *Nature*, vol. 261, pp. 402–403, June 1976.

30. B. O'Regan and M. Grätzel, "A low-cost, high-efficiency solar cell based on dye-sensitized colloidal TiO_2 films," *Nature*, vol. 353, pp. 737–740, Oct. 1991.

31. H. J. Snaith and L. Schmidt-Mende, "Advances in Liquid-Electrolyte and Solid-State Dye-Sensitized Solar Cells," *Advanced Materials*, vol. 19, pp. 3187–3200, Sept. 2007.

32. U. Bach, P. Comte, J. E. Moser, F. Weisso, and M. Gra, "Solid-statedye-sensitized mesoporous TiO_2 solar cells with high photon-to-electron conversion efficiencies," *Nature*, vol. 395, pp. 583–585, 1998.

33. J. Krüger, R. Plass, M. Grätzel, P. J. Cameron, and L. M. Peter, "Charge transport and back reaction in solid-state dye-sensitized solar cells: A study using intensity-modulated photovoltage and photocurrent spectroscopy," *The Journal of Physical Chemistry B*, vol. 107, no. 31, pp. 7536–7539, 2003.

34. Y. Tachibana, J. E. Moser, M. Grätzel, D. R. Klug, and J. R. Durrant, "Subpicosecond Interfacial Charge Separation in Dye-Sensitized Nanocrystalline Titanium Dioxide Films," *The Journal of Physical Chemistry*, vol. 100, no. 51, pp. 20056–20062, 1996.

35. N. A. Anderson and T. Lian, "Ultrafast electron injection from metal polypyridyl complexes to metal-oxide nanocrystalline thin films," *Coordination Chemistry Reviews*, vol. 248, no. 13-14, pp. 1231–1246, 2004.

36. U. Bach, Y. Tachibana, J.-E. Moser, S. A. Haque, J. R. Durrant, M. Grätzel, and D. R. Klug, "Charge Separation in Solid-State Dye-Sensitized Heterojunction Solar Cells," *Journal of the American Chemical Society*, vol. 121, no. 32, pp. 7445–7446, 1999.

37. D. Kuang, C. Klein, H. J. Snaith, J.-E. Moser, R. Humphry-Baker, P. Comte, S. M. Zakeeruddin, and M. Grätzel, "Ion Coordinating Sensitizer for High Efficiency Mesoscopic Dye-Sensitized Solar Cells: Influence of Lithium Ions on the Photovoltaic Performance of Liquid and Solid-State Cells," *Nano Letters*, vol. 6, no. 4, pp. 769–773, 2006.

38. J. Orenstein and M. Kastner, "Photocurrent transient spectroscopy: Measurement of the density of localized states in *a* -as_2se_3," *Phys. Rev. Lett.*, vol. 46, pp. 1421–1424, May 1981.

39. T. Tiedje and A. Rose, "A physical interpretation of dispersive transport in disordered semiconductors," *Solid State Communications*, vol. 37, no. 1, pp. 49–52, 1981.

40. C. J. Barbé, F. Arendse, P. Comte, M. Jirousek, F. Lenzmann, V. Shklover, and M. Grätzel, "Nanocrystalline titanium oxide electrodes for photovoltaic applications," *Journal of the American Ceramic Society*, vol. 80, no. 12, pp. 3157–3171, 1997.

41. P. M. Sommeling, B. C. O'Regan, R. R. Haswell, H. J. P. Smit, N. J. Bakker, J. J. T. Smits, J. M. Kroon, and J. A. M. van Roosmalen, "Influence of a $TiCl_4$ Post-Treatment on Nanocrystalline TiO_2 Films in Dye-Sensitized Solar Cells," *The Journal of Physical Chemistry B*, vol. 110, no. 39, pp. 19191–19197, 2006.

42. B. C. O'Regan, J. R. Durrant, P. M. Sommeling, and N. J. Bakker, "Influence of the $TiCl_4$ Treatment on Nanocrystalline TiO_2 Films in Dye-Sensitized Solar Cells. 2. Charge Density, Band Edge Shifts, and Quantification of Recombination Losses at Short Circuit," *The Journal of Physical Chemistry C*, vol. 111, no. 37, pp. 14001–14010, 2007.

43. A. Abate, T. Leijtens, S. Pathak, J. Teuscher, R. Avolio, M. E. Errico, J. Kirkpatrik, J. M. Ball, P. Docampo, I. McPherson, and H. J. Snaith, "Lithium salts as "redox active" p-type dopants for organic semiconductors and their impact in solid-state dye-sensitized solar cells," *Physical chemistry chemical physics : PCCP*, vol. 15, pp. 2572–9, Feb. 2013.

44. J. Kroeze, N. Hirata, L. Schmidt-Mende, C. Orizu, S. Ogier, K. Carr, M. Grätzel, and J. Durrant, "Parameters Influencing Charge Separation in Solid-State Dye-Sensitized Solar Cells Using Novel Hole Conductors," *Advanced Functional Materials*, vol. 16, no. 14, pp. 1832–1838, 2006.

45. P. Wang, S. Zakeeruddin, R. Humphry-Baker, J. Moser, and M. Grätzel, "Molecular-Scale Interface Engineering of TiO_2 Nanocrystals: Improve the Efficiency and Stability of Dye-Sensitized Solar Cells," *Advanced Materials*, vol. 15, no. 24, pp. 2101–2104, 2003.

46. M. A. Green, K. Emery, Y. Hishikawa, W. Warta, and E. D. Dunlop, "Solar cell efficiency tables (version 43)," *Progress in Photovoltaics: Research and Applications*, vol. 22, no. 1, pp. 1–9, 2014.

47. A. Kojima, K. Teshima, Y. Shirai, and T. Miyasaka, "Organometal halide perovskites as visible-light sensitizers for photovoltaic cells," *Journal of the American Chemical Society*, vol. 131, no. 17, pp. 6050–6051, 2009.

48. M. M. Lee, J. Teuscher, T. Miyasaka, T. N. Murakami, and H. J. Snaith, "Efficient hybrid solar cells based on meso-superstructured organometal halide perovskites.," *Science (New York, N.Y.)*, vol. 338, pp. 643–7, Nov. 2012.

49. J.-H. Im, C.-R. Lee, J.-W. Lee, S.-W. Park, and N.-G. Park, "6.5% efficient perovskite quantum-dot-sensitized solar cell," *Nanoscale*, vol. 3, pp. 4088–4093, 2011.

50. J. Burschka, N. Pellet, S.-J. Moon, R. Humphry-Baker, P. Gao, M. K. Nazeeruddin, and M. Grätzel, "Sequential deposition as a route to high-performance perovskite-sensitized solar cells.," *Nature*, vol. 499, pp. 316–9, July 2013.

51. National Renewable Energy Laboratory, "Research cell efficiency records chart." `http://www.nrel.gov/ncpv/images/efficiency_chart.jpg`, May 2014.

52. A. Nozik, "Quantum dot solar cells," *Physica E: Low-dimensional Systems and Nanostructures*, vol. 14, pp. 115–120, Apr. 2002.

53. J. H. Rhee, C.-C. Chung, and E. W.-G. Diau, "A perspective of mesoscopic solar cells based on metal chalcogenide quantum dots and organometal-halide perovskites," *NPG Asia Materials*, vol. 5, p. e68, Oct. 2013.

54. O. E. Semonin, J. M. Luther, S. Choi, H.-Y. Chen, J. Gao, A. J. Nozik, and M. C. Beard, "Peak External Photocurrent Quantum Efficiency Exceeding 100via MEG in a Quantum Dot Solar Cell," *Science*, vol. 334, no. 6062, pp. 1530–1533, 2011.

55. P. P. Boix, G. Larramona, A. Jacob, B. Delatouche, I. Mora-Seró, and J. Bisquert, "Hole transport and recombination in all-solid sb2s3-sensitized tio2 solar cells using cuscn as hole transporter," *The Journal of Physical Chemistry C*, vol. 116, no. 1, pp. 1579–1587, 2012.

56. ASTM Standard G173, 03(2013), *Standard Tables for Reference Solar Spectral Irradiances: Direct Normal and Hemispherical on 37° Tilted Surface*. West Conshohocken, PA: ASTM International, 2012.

57. B. A. Gregg, "Excitonic Solar Cells," *The Journal of Physical Chemistry B*, vol. 107, pp. 4688–4698, May 2003.

58. B. G., C. H., and V. J., *Materials Handbook*. New York: Mcgraw-Hill Handbooks, 5th ed., 2002.

59. Y. Wang, J. Chen, P. Wang, L. Chen, Y.-b. Chen, and L.-m. Wu, "Syntheses, Growth Mechanism, and Optical Properties of [001] Growing Bi 2 S 3 Nanorods," *The Journal of Physical Chemistry C*, vol. 113, pp. 16009–16014, Sept. 2009.

60. R. Malakooti, L. Cademartiri, Y. Akçakir, S. Petrov, A. Migliori, and G. A. Ozin, "Shape-Controlled Bi2S3 Nanocrystals and Their Plasma Polymerization into Flexible Films," *Advanced Materials*, vol. 18, pp. 2189–2194, Aug. 2006.

61. M. V. Kovalenko, M. Scheele, and D. V. Talapin, "Colloidal Nanocrystals with Molecular Metal Chalcogenide Surface Ligands," *Science*, vol. 324, no. 5933, pp. 1417–1420, 2009.

62. G. Konstantatos, L. Levina, J. Tang, and E. H. Sargent, "Sensitive solution-processed Bi2S3 nanocrystalline photodetectors.," *Nano letters*, vol. 8, pp. 4002–6, Nov. 2008.

63. R. Vogel, P. Hoyer, and H. Weller, "Quantum-Sized PbS, CdS, Ag2S, Sb2S3, and Bi2S3 Particles as Sensitizers for Various Nanoporous Wide-Bandgap Semiconductors," *The Journal of Physical Chemistry*, vol. 98, pp. 3183–3188, Mar. 1994.

64. L. Martinez, A. Stavrinadis, S. Higuchi, S. L. Diedenhofen, M. Bernechea, K. Tajima, and G. Konstantatos, "Hybrid solution-processed bulk heterojunction solar cells based on bismuth sulfide nanocrystals.," *Physical chemistry chemical physics : PCCP*, vol. 15, pp. 5482–7, Apr. 2013.

65. Y. Liu, M. Gibbs, J. Puthussery, S. Gaik, R. Ihly, H. W. Hillhouse, and M. Law, "Dependence of Carrier Mobility on Nanocrystal Size and Ligand Length in PbSe Nanocrystal Solids," *Nano Letters*, vol. 10, no. 5, pp. 1960–1969, 2010.

66. H. J. Snaith, "The perils of solar cell efficiency measurements," *Nature Photonics*, vol. 6, pp. 337–340, May 2012.

67. M. T. S. Nair, L. Guerrero, and P. K. Nair, "Conversion of chemically deposited CuS thin films to and by annealing," *Semiconductor Science and Technology*, vol. 13, pp. 1164–1169, Oct. 1998.

68. E. Maier, A. Fischereder, W. Haas, G. Mauthner, J. Albering, T. Rath, F. Hofer, E. J. List, and G. Trimmel, "Metal sulfide–polymer nanocomposite thin films prepared by a direct formation route for photovoltaic applications," *Thin Solid Films*, vol. 519, pp. 4201–4206, Apr. 2011.